J. Fluid Mech. (1989), *vol.* 209, *pp.* 93–150
Printed in Great Britain

Resonant growth of three-dimensional modes in transitioning Blasius boundary layers

By T. C. CORKE AND R. A. MANGANO

Illinois Institute of Technology, Fluid Dynamics Research Center, Mechanical and Aerospace Engineering Department, Chicago, IL 60616, USA

(Received 23 August 1988 and in revised form 19 May 1989)

By carefully controlled phase-coupled input of simultaneous two- and three-dimensional disturbances, the nonlinear evolution and breakdown of the laminar flow in a boundary layer was examined. This involved the generation of plane Tollmien–Schlichting waves and pairs of oblique waves so as to promote near-resonance conditions which have been theoretically shown to lead to the rapid development of three-dimensionality in unstable boundary layers. Special emphasis is placed on the two prominent mechanisms, namely resonant-triads of Orr–Sommerfeld modes and the secondary instability of the streamwise periodic flow to spanwise periodic three-dimensional disturbances. The sensitivity of these mechanisms on the amplitudes and wavenumbers of the input disturbances was of special focus.

The simultaneous two- and three-dimensional wave generation was accomplished using a spanwise array of line heaters suspended just above the wall at the approximate height of the critical layer in the laminar boundary layer. These were operated to produce, through local heating, time-periodic spanwise-phase-varying velocity perturbations. Of primary emphasis in this paper are conditions obtained by the combined forcing of fundamental plane waves with wavenumbers $(\alpha, 0)$ and pairs of subharmonic oblique waves $(\frac{1}{2}\alpha, \pm\beta)$. The results document resonant growth of energy in the subharmonic modes, the formation of staggered lambda vortex patterns with a cross-stream scale commensurate with the seeded $\pm\beta$ condition, and their subsequent transition to turbulence. Complete documentation of the flow field at these various stages is presented using smoke-wire flow visualization and through phase-conditioned hot-wire surveys measuring all three velocity components in three space dimensions.

1. Introduction

Experiments on boundary-layer transition performed in low-disturbance wind tunnels have established three basic regimes of breakdown from laminar to turbulent flow. The first regime consists of plane Tollmien–Schlichting (TS) waves which are invariant in the spanwise direction and propagate with the flow. The frequencies and growth rates of these waves are readily predicted from linear stability theory. In the second regime, spanwise-periodic three-dimensional deformations of the nominally two-dimensional TS waves appear. In the third regime, rapid streamwise stretching and secondary instabilities of the lifted three-dimensional structures lead to the generation of smaller scale random motions and the final stages of breakdown. The subject of this paper is the final two regimes in the path to turbulence, in particular the initially weakly *nonlinear processes* leading to the growth of large-amplitude strongly nonlinear three-dimensional disturbances and transition to turbulence.

1.1. *Background*

The most commonly cited early experiments which have focused on the development of three-dimensionality in unstable boundary layers are due to Klebanoff & Tidstrom (1959) and Klebanoff, Tidstrom & Sargent (1962). In their pioneering investigations, they established the existence of downstream-growing spanwise variations in the mean and fluctuating velocity components and their fundamental role in the consistent features of the developing instability. In addition they made attempts, in one of the first applications of transition control in boundary layers, to locally fix the significant three-dimensional (3-D) features of turbulent breakdown by creating artificial disturbances of spanwise periodic nature. Under reasonably large two-dimensional (2-D) input intensities (order of 1% u'/U_∞), they documented the warping of initially plane TS waves into peak–valley pairs which were aligned in the flow direction. This yielded a particularly catastrophic breakdown characterized by the sudden appearance of 'spikes' in the time traces of streamwise velocity fluctuations and the growth of high-frequency oscillations and turbulent 'spots'. As a result of the detailed description of this process given by Klebanoff *et al.* (1962), it has come to be called K-type breakdown or K-type modes (Herbert & Morkovin 1980).

The initial experimental results of Klebanoff & Tidstrom (1959) and later of Hama (1960) sparked early theoretical attempts to model the progressive growth of three-dimensionality in boundary layers. Benney & Lin (1960) and later Benney (1964), considered the second-order nonlinear interaction of 2-D TS waves with 3-D waves of a given spanwise periodicity. They found that such interactions promoted the growth of spanwise periodic longitudinal vortical patterns which were qualitatively similar to the K-type modes. Although the Benney–Lin model pointed to a mechanism for the observed growth of three-dimensionality in unstable boundary layers, it furnished no estimate of the preferred spanwise periodicity observed in the experiments.

As a result of this and other more serious shortcomings, Craik (1971) proposed a model that would favour the selective growth of three-dimensional disturbances. This involved resonant interactions among a suitable triad of TS waves. Such interactions were expected to be quite strong owing to a phase-coupled energy interchange among wave components with the potential transfer of energy from the primary shear flow to the disturbance in the region of the critical layer. The importance of resonant subharmonic wave interactions in free shear layers had been pointed out by Kelly (1968). This was found (Corke, Shakib & Nagib 1989) to be an important mechanism governing the initial growth of instabilities and feedback in jets.

The Craik model considered the disturbance field to be the result of a plane TS wave and two oblique TS waves propagating at equal and opposite angles to the flow direction in the form of a triad. Resonance occurs when the phase velocities of the wave components are matched. This generally involves the most amplified 2-D TS wave with wavenumber α, and pairs of oblique waves with a streamwise wavenumber $\frac{1}{2}\alpha$.

The Craik model provided a mechanism for selective amplification of a pair of oblique waves even in situations where such waves may be damped according to linear theory. Since it involves the subharmonic, it is often referred to as a subharmonic interaction, and is often implied when describing Craik or 'C-type' modes. Although the motivation for the Craik analysis was to provide a mechanistic interpretation of the Klebanoff *et al.* observations, the model proved to be inadequate. Craik (1971) surmised that the too large 2-D disturbance amplitudes introduced by the vibrating ribbon in that experiment resulted in higher-order effects not accounted for in his theory. Although not successful in this regard, Craik's analysis did reveal the existence of this particularly strong second-order resonance mechanism which may be more directly relevant to the early stages of natural (not artificially forced) transition.

The first experimental observance of a TS subharmonic in a transitioning boundary layer was made by Kachanov, Koslov & Levchenko (1977). The subharmonic was determined from spectra of streamwise velocity fluctuations. The streamwise phase distributions between the fundamental TS and subharmonic modes, necessary to show resonance, were unfortunately lacking. Further investigations by Kachanov & Levchenko (1984), however, provided detailed phase and amplitude distributions documenting the existence of a synchronized phase locking between a 2-D TS wave and a pair of oblique waves propagating at equal and opposite angles to the flow. Kachanov & Levchenko believed this to be evidence of the Craik modes even though the angles of the subharmonic oblique waves differed substantially from the theoretical value satisfying the Orr–Sommerfeld equation. Irrespective of this difference (a possible explanation is provided by Herbert 1983*b*), the resonant growth of the subharmonic disturbance – far in excess of that predicted by linear theory – was fully apparent.

Kachanov & Levchenko had further observed that the parametric resonance not only led to the amplification of the TS subharmonic but also to the growth of a broad band of lower frequency disturbances. This they felt was tied to an observed stochastic modulation of the phase and amplitude of the subharmonic time trace which set up lower frequency sum and difference interactions. They surmised that the modulated subharmonic arose from random background disturbances, and attempted to document this process by superposing on their 2-D ribbon input a phase-modulated subharmonic signal. The resulting resonant condition under 2-D subharmonic forcing corresponded, within the experimental uncertainties, to those obtained when only natural random priming of the subharmonic existed. This result is not altogether unexpected since the growth of 2-D subharmonic disturbances is damped and would probably have little influence on the growth of 3-D disturbances in the regime where TS wave amplitudes are small.

With the aid of a smoke wire (Corke *et al.* 1977), Saric & Thomas (1983) performed experiments on the growth of subharmonic disturbances in unstable boundary layers. From their flow visualization records, it was clear that the streamwise subharmonic arose from a formed peak–valley structure, whereby peaks followed valleys and valleys followed peaks. Thus a sensor monitoring the streamwise velocity fluctuations along a mean stream path would detect the passage of peaks or valleys spaced two TS wavelengths apart, i.e. a TS subharmonic. By varying the initial amplitude of the TS forcing, they had observed the emergence of subharmonic modes with different spanwise wavelengths (λ_z). From that they distinguished between C-type and H-type mechanisms.

An explanation of the H-type modes comes from the analysis of Herbert (1983*b*). He examined the stability to 3-D disturbances of a basic state consisting of a Blasius flow and plane TS waves. The unstable 3-D disturbances were found to be Squire modes, not Orr–Summerfeld modes as in the case of the Craik mechanism. The same modes of the Squire equations were observed by Herbert (1983*a*) to cause the subharmonic instability in Poiseuille flow. By this mechanism, the phase velocity of the 3-D modes is independent of the spanwise wavenumber, $\beta = 2\pi/\lambda_z$, and is close to that of the fundamental TS wave. Therefore, near-resonant conditions could exist independent of β, as opposed to the C-type modes which only exist for unique values of spanwise wavenumbers. An excellent recent review of this topic was given by Herbert (1988).

1.2. *Objectives*

In the light of the important theoretical contributions on the weakly nonlinear interactions leading to the growth of 3-D disturbances in transitioning boundary layers, we proposed to expand on the previously cited experiments by adding the capability for introducing *controlled 3-D inputs*. These 3-D disturbances would take the form of oblique waves of different angles and intensities, which would be phase coupled to simultaneously generated 2-D disturbances. The simultaneous generation of both 2-D and oblique modes would prescribe an initial phase synchronism between the modes. As emphasized earlier, previous experimental studies have left this phase synchronism to develop naturally through coupling with background 3-D disturbances.

With this, we intended to look at the two basic mechanisms for the growth of 3-D *subharmonic modes*, and in addition, to address the apparent differences in the structure of breakdown between fundamental-mode (K-type) and subharmonic-mode breakdown (C- and H-type) conditions. For example, total u'/U_∞ values documented for K-type conditions are of the order of 15%. In C- or H-type breakdown, the level is typically observed to be an order of magnitude smaller. More fundamentally, for the K-type, the appearance of spike stages puts greater emphasis on higher frequency generation at breakdown, whereas measurements of C- or H-type transition suggests that interaction with low-frequency components is more important.

2. Experimental apparatus

2.1. *Wind tunnel*

The experiment was performed in the IIT Transition Wind Tunnel, a schematic of which is shown in figure 1. The same facility had been previously used by Bar-Sever (1984) and Corke, Bar-Sever & Morkovin (1986), to study the instability and transition to turbulence of boundary layers over random grain surface roughness. Details of the facility can be found in those two references.

The test section dimensions are 73.7 cm by 15.1 cm cross-section by 2.5 m long. One sidewall acted as a measurement surface upon which the Blasius layer was developed. This wall was constructed from two sheets of 20 gauge, 430 series stainless steel bonded on each side of a 2.5 cm thick honeycomb core. This formed one continuous, extremely flat and durable surface over the full height and length of the test section. This surface was smooth to a nearly optical-mirror quality without the need for polishing. This proved to be a great advantage when introducing lighting for flow visualization.

A false floor and ceiling in the test section were part of a special treatment to inhibit the growth of any disturbances attributed to three-dimensional corner flows. By that arrangement, seen in figure 1(*b*), a slightly higher static pressure was maintained in the measurement section, set up by a perforated grid at the downstream end. The difference in pressure between the measurement section and

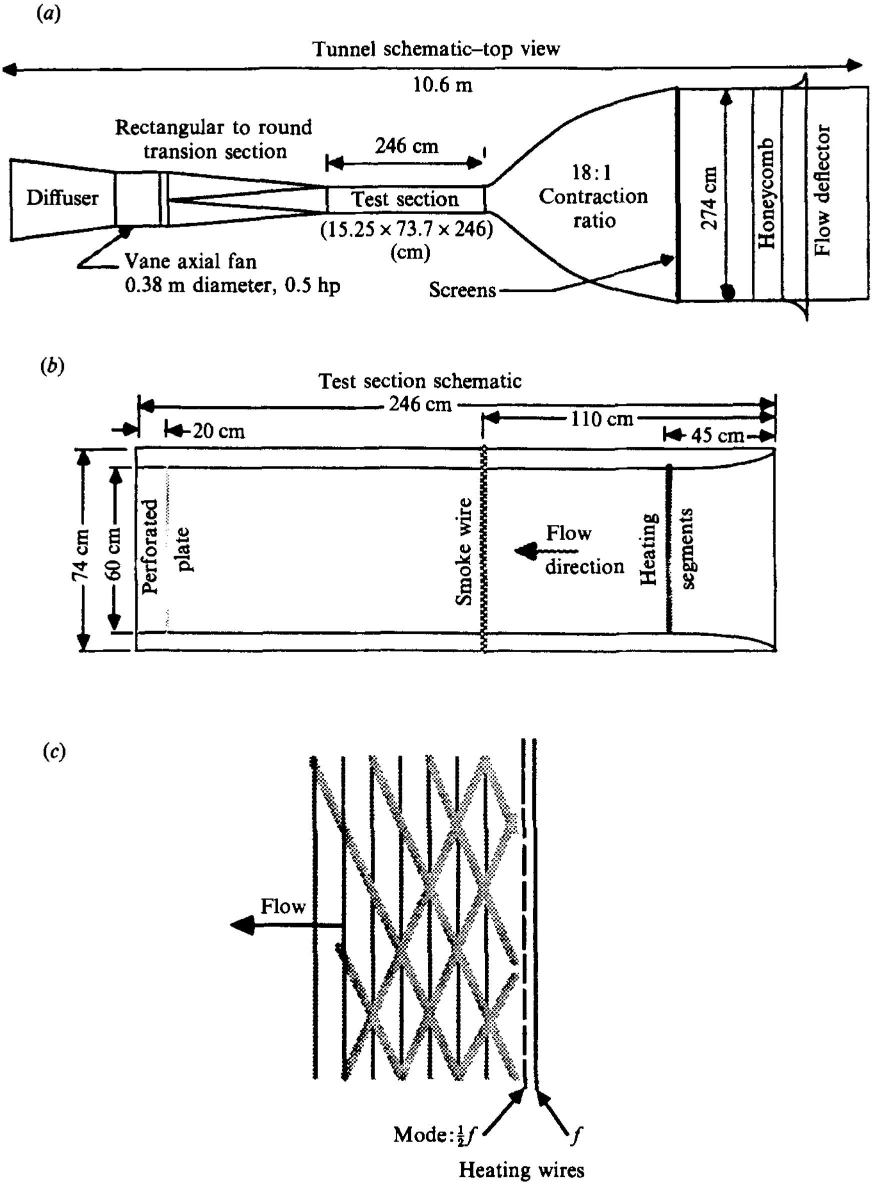

FIGURE 1. Schematic drawing of (a, b) boundary-layer-transition wind tunnel and test section and (c) heating wire arrangement for seeding combined TS and oblique wave modes.

the false ceiling and floor cavities caused fluid to be drawn off through small gaps at the corners. The gap openings were adjusted while visualizing the flow using a smoke-wire and monitoring the two-dimensionality of TS modes and degree of three-dimensional modes near the corners. With a moderate amount of iterations, very satisfactory suppression of corner disturbances could be achieved.

The other sidewall of the test section was either a single section of clear Plexiglas, used when visualizing the flow, or a segmented access window used for introducing velocity probes. These probes were traversed by a computer-controlled motorized tri-axial traversing mechanism which was mounted outside the test section. In the

y-direction (normal to the wall) a minimum resolvable displacement of 0.01 mm, or approximately 100 times smaller than the average boundary-layer thickness, was possible.

2.2. *Flow visualization*

For flow visualization, a sheet of smoke streaklines was introduced near the wall using the smoke-wire technique (Corke *et al.* 1977). The smoke wire consisted of a 0.1 mm diameter wire which was suspended and held taut above the measurement wall by two support arms. The support arms were located outside the measurement portion of the test section, within the ceiling and floor cavities, so that they would not introduce a disturbance to the flow. The distance of the smoke wire from the measurement wall was adjustable. This control was essential since the patterns that developed were dependent on the height at which the smoke was introduced. In this experiment, the smoke wire was placed at the height of the critical layer in order to best mark the instability waves and emerging structures associated with the transition process. Lighting was provided by strobe lights positioned next to the test section. These were oriented so that the light would obliquely reflect off the mirror-like measurement wall. Under this arrangement, with the camera viewpoint normal to the wall and in the absence of smoke, the field of view appeared black. Smoke streaks which convected into the field of view diffused the light and therefore appeared white on the otherwise black background.

2.3. *Instrumentation*

The basic instrumentation used in the experiment performed the tasks of providing voltage time series proportional to the three components of velocity, amplification of these, various stages of analog preprocessing and data reduction, signal conditioning, and interfacing to computer analog-to-digital inputs. A primary goal reflected in the design of the set-up was the need to precisely set the forcing conditions from day to day, and to provide a real-time evaluation of the state of the flow. Equally important, the electronics were required to provide signals which could maintain the highest resolution possible to the A/D converted under conditions where the amplitude of velocity fluctuations taken at different points in space could vary by three orders of magnitude.

Hot-wire sensors were constructed from 0.00375 mm diameter tungsten wire. Copper was electroplated to the ends of the wire to provide an effective sensor length of 0.5 mm. These wires were soldered to 4 cm long (approximately four times the maximum boundary-layer thickness) fine diameter jewellers broaches in three basic configurations designed to measure different velocity components, primarily u, uv, or uw. The long broach lengths were necessary to ensure that probes, when traversed normal to the wall, produced a minimum disturbance due to the larger diameter probe body. The sensitivity of such unstable boundary-layer flows to probe-body interference had been documented by Bar-Sever (1984). Small-diameter glass fibres spanned between the thin broaches at their midlength in order to stabilize them to flow-induced vibrations. The complete sensor design is given by Mangano (1987).

In all cases the hot-wire sensors were operated in a constant-temperature mode using DISA 55D01 anemometer units. Prior to digitizing, the analog outputs of each anemometer were split into two parts, one containing a d.c. component proportional to the mean velocity and the other which was d.c. removed and proportional to the velocity fluctuations. The signal containing the d.c. was d.c. shifted and amplified by the full amount possible, within the ±10 V limit of the A/D converter. The dominant factor in the selection of the gain was the d.c. variation over a y-traverse through the layer. The gain on this signal was fixed. This signal was then passed to one channel of the A/D input.

The other signal was band-pass filtered between 1.25 Hz and 160 Hz. The low-pass setting acted as an anti-aliasing filter for the digital acquisition rate of 384 Hz or 432 Hz (24 times the oblique wave frequency). The filtered signal then passed through a computer-controlled programmable gain circuit. When acquired through a separate channel of the A/D, the computer always acted to maintain the highest gain for a sample record in order to minimize quantization error of the digitized values. That gain setting was used to reconstruct the total signal when the mean value was added back to the fluctuating part, with floating point precision, within the computer memory.

3. Controlled three-dimensional mode forcing

The simultaneous 2-D and 3-D wave generation was accomplished using an array of 0.05 mm diameter heating wires suspended at the height of the critical layer. These were periodically heated to introduce controlled perturbations through local changes in the air viscosity. The oblique waves were produced by using a spanwise array of individual heating wires. Such an array is schematically represented in figure 1(*c*).

3.1. *Periodic local heating*

The use of periodic heating to introduce controlled disturbances had been used by Liepmann, Brown & Nosenchuck (1982) to force plane TS waves in boundary layers in water. In their case, they used a two-dimensional heating element made from a 2.5 mm wide (in the flow direction) nichrome strip mounted flush to the boundary-layer wall. In that reference, the analogy between periodic heating/cooling and surface blowing/suction was made to give an equivalent effect on the vertical velocity component. The v/U_∞ dependence given by them was

$$\mathrm{abs}\left(\frac{v}{U_\infty}\right) \propto \frac{Pr^{\frac{1}{3}}}{Re_x^{\frac{1}{2}}}\frac{x^{\frac{1}{3}}}{\xi^{\frac{1}{3}}}\frac{T}{\mu}\frac{\mathrm{d}\mu}{\mathrm{d}T}\frac{\Delta T}{T}.$$

For the estimated conditions of Liepmann *et al.* (1982), in water, with the distance from virtual origin $x = 5.0$ cm, heating strip streamwise extent $\xi = 2.54$ mm, local stability Reynolds number $Re_x^{\frac{1}{2}} = 316$, Prandtl number $Pr = 7.1$; ambient temperature $T = 20$ °C, and temperature/viscosity sensitivity $(T/\mu)(\mathrm{d}\mu/\mathrm{d}T) = 0.51$, the v/U_∞ equivalence to a temperature perturbation amplitude ΔT (°C) was

$$\mathrm{abs}\left(\frac{v}{U_\infty}\right) = 0.0004\Delta T.$$

In water, the local high dependence of viscosity on temperature required moderately low temperature amplitudes to force disturbances. The ΔT value used by Liepmann *et al.* (1982) was estimated to be 3 °C. For the present case, in air, an approximate factor-of-five reduction in $(T/\mu)(\mathrm{d}\mu/\mathrm{d}T)$ and a factor-of-two reduction in $Pr^{\frac{1}{3}}$, between air and water, requires that an approximately ten times larger temperature fluctuation amplitude be used to obtain the same level of velocity perturbation. This assumes that the heating segments have the same physical streamwise width. Such high fluctuating temperatures are generally unrealistic since some portion is averaged and stored by the wall substrate leading to a local steady increase in the boundary-layer temperature. In air, this effect is stabilizing.

However, an improvement in this factor can be realized by reducing the streamwise extent of a heating segment, that is replacing strips by wires.

In the present experiment in air, heating elements consisting of 0.05 mm diameter wires, for the conditions $x = 45$ cm, $\xi = 0.05$ mm, $Re^{\frac{1}{2}}_x = 430$, $Pr = 0.71$, $T = 20$ °C and $(T/\mu)(\mathrm{d}\mu/\mathrm{d}T) = 0.119$ yield a perturbation intensity dependence of

$$\mathrm{abs}\left(\frac{v}{U_\infty}\right) = 0.0003\Delta T.$$

Therefore, under these conditions, temperature perturbation amplitudes which were comparable with those used in water could be used for the present experiment in air.

3.2. *Oblique mode generation*

The oblique wave generation was accomplished by using a spanwise array, at one x-location, of individual heating wires to produce time-periodic spanwise-phase-varying perturbations. In such an application, for an individual heating segment of length s, a periodic time-series input period τ, and a radian phase shift between adjacent heating wires ϕ, spatially propagating waves would be produced with a wave angle θ given by

$$\theta = \arctan\,(C_\mathrm{r}\,\phi\tau/2\pi s).$$

Here C_r is the streamwise phase velocity of the travelling oblique waves. Keeping the length of the wire-heater segments fixed, at a given phase velocity set by the free-stream speed, τ and ϕ could be adjusted to produce waves at any desired angle.

Pairs of waves with equal wave angles and opposite sign were produced by spanwise phase distributions which were symmetric about the centre span of the heating-wire array. Such wave pairs, along with a harmonic plane TS mode, formed wave triads such as shown in figure 1 (*c*).

In terms of the dimensionless wavenumbers, α and β, the wave angle is given by

$$\theta = \arctan\,(\beta/\alpha).$$

In terms of the experimental parameters,

$$\beta/\alpha = C_\mathrm{r}\,\phi\tau/2\pi s.$$

A two-dimensional wave, $(\alpha, 0)$, for example, requires an input condition with $\phi = 0$, that is, a spanwise uniform input to all wire heaters.

In the implementation of this approach we utilized 15 wire segments, each of length 3.8 cm. These were placed end to end to span the full width of the measurement section. At the operating velocity of 6 m/s and a highest 3-D subharmonic frequency of interest of 18 Hz, this system was capable of producing oblique wave angles of up to 61°. These were produced at the limiting phase shift, $\phi = \pi$. In the course of this we have halved and doubled the number of wire segments. In the former case, the longer segment lengths limited the maximum wave angles to values which were less than those needed to produce the most amplified 3-D modes. Although the latter offered steeper angle capability, as will become apparent, the computer interfacing favoured 15 segments.

The individual heating segments were made from 0.05 mm diameter stainless steel wire. The ends of each wire were copper plated to produce a central portion, equal to the segment length s, of higher resistance, where the actual heating took place. A special low-heat-conduction substrate (Ardel) was inset into the back wall directly under the heating segments to minimize conductive losses and electrically insulate the individual wires. Pairs of holes were drilled through the Ardel sheet to accommodate the 15 heating wires. The holes were located to space the wires ends 1.6 mm ($\frac{1}{24}$ s) apart. The centre of the eighth, or symmetry, wire segment coincided with the tunnel centreline ($z = 0$).

In early configurations, the wire segments were placed on the wall surface. In the final configuration, for the results presented here, the heating wires were suspended 0.2 mm off the wall surface. This corresponded to the approximate height of the critical layer for the range of Reynolds numbers used. Using the local velocity, the Reynolds number based on the wire diameter was subcritical. The wires were held away from the wall by 0.6 mm outer diameter stainless steel tubes that were inserted through the wire holes in the Ardel. These were glued in place to provide the required clearance. The plated ends of the wires were then passed through these tubes and secured to the backside of the Ardel with screws. The wires were placed in tension by wrapping them around the screws before tightening. All electrical connections were made outside the tunnel test section on the backside of the measurement wall.

A separate single 2-D heating wire spanning the width of the measurement section was placed 3 mm upstream of the 3-D segments. This wire was also suspended above the Ardel surface, at the slightly higher distance from the wall of 0.5 mm. A miniature temperature sensor located 3 mm downstream of the heating wires on the spanwise centreline was used to monitor the unsteady heating amplitudes.

3.3. *Control hardware*

The time-series wave form used to provide the periodic heating current to the wire segments was chosen to be a half-rectified square wave. This was selected over a unrectified sine wave, such as used by Liepmann *et al.* (1982), because the square wave only requires a changing output state which can be more easily produced by a computer or digital logic circuits. This was important for applications such as ours where a single processor controls the clocking of inputs to the 16 heating wires, and simultaneously moves sensors, acquires and pre-processes sensor outputs.

This was done by controlling the state of the 16-wire segment through 1 bit each of a 16-bit parallel interface (15 bits for the 3-D segments, 1 bit for the 2-D segment). These were connected through two stages of circuitry which provided low power isolation and current amplification while preserving the half-rectified character of the parallel interface output. Approximately 1 W/cm of heating wire was required to reach the perturbation intensities needed in the experiment. Details of these circuits are contained in Mangano (1987). By this approach, the states of all 16 heating wires could be changed simultaneously by transferring a single 16-bit word to the parallel output.

The amplitude levels for the 3-D wires (as a group) and the 2-D wire were controlled separately using individual d.c. voltage sources. This was an important capability to have in order to investigate the effect of initial amplitudes on mode selection by Saric & Thomas (1983). The 15 3-D wires were connected in parallel to a single d.c. source. Any spanwise non-uniformity in heating amplitude between segments was minimized by matching their resistance values, set by the non-plated lengths.

3.4. *Control software*

The heating-segment control software was designed to be a user-interactive program which could provide different 2-D wave frequencies, 3-D wave frequencies and angles, phase shifts between 2- and 3-D waves, and forcing time-series duty cycles.

In order to represent phase increments in the square wave, the period was divided

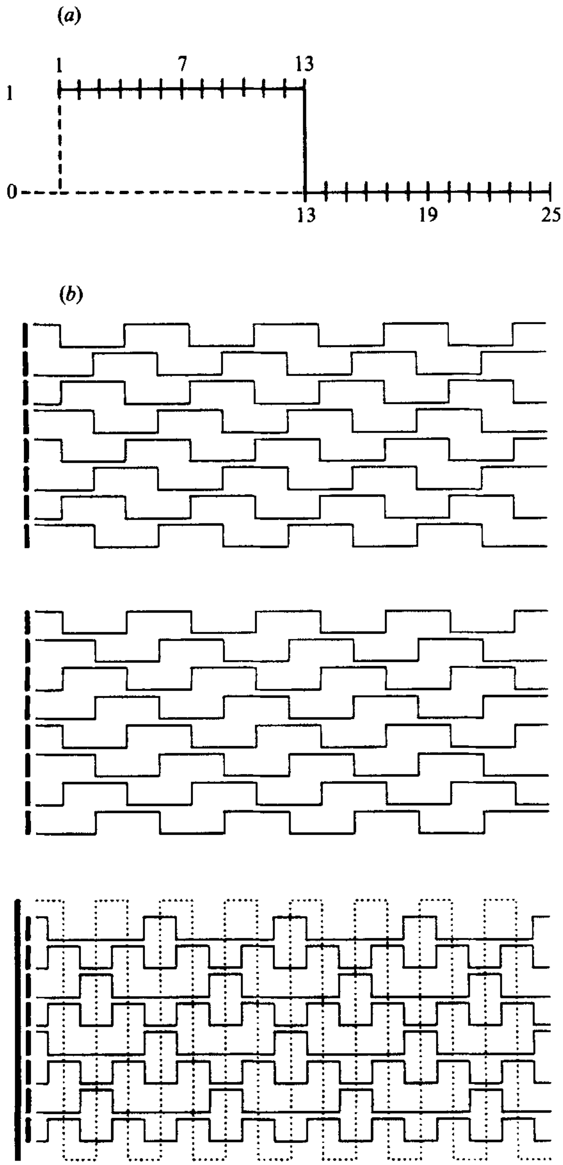

FIGURE 2. Schematic showing one cycle of periodic disturbance input broken into 25 parts to provide discreet phase shifts between heating wire segments (*a*), and sample time series used to produce 90P condition (*b*).

into 24 parts. This was taken to be the minimum phase increment corresponding to 15°. A single period of the wave form, in figure 2(*a*), would represent a single period of the signal output to *one* of the 3-D heating wires. To produce a phase shift, ϕ, between adjacent heating wires, required a similar square wave shifted in time (phase) relative to the other. For example, an output series shifted by 90° was shifted by seven phase increments. Single periods with appropriate phase shifts corresponding to the control time series for all 16 wire heating segments were produced in the same manner. The state of each of the wire segments at each instant, corresponding to $\frac{1}{24}$th of a period, was stored in one bit of a 16-bit digital word. Successive instants in time were stored in successive memory locations.

The digital words containing the states of each segment were sequentially loaded into the output register of the parallel interface. The rate at which these digital words were sent was controlled by a programmable clock operating at a rate that was 24 times the 3-D mode frequency. This produced the desired oblique mode frequency (divided into 24 parts) and the desired 2-D (TS) mode frequency divided into the number of parts commensurate with the ratio of 2-D and 3-D frequencies.

In figure 2(*b*) are presented sample time series outputs for the 3-D and 2-D segments to produce 45° waves. For our experimental conditions this requires a 90° phase shift between 3-D segments. Because of symmetry, only half of the 15 segments, represented as bold lines, are shown in this figure. The top set corresponds to the spanwise phase distribution necessary to produce waves of positive angle. The middle set corresponds to the distribution necessary to produce wave pairs of equal and opposite angles. Since we were interested in producing wave triads, the two patterns were added (logically or-ed) together to produce equal and opposite wave pairs. The problem in performing that operation is apparent for wire segment numbers 1, 3, 5 and 7 in that figure. In those cases, adding the wave forms leaves those segments at a high state (heating) for all time steps, a physically unrealistic condition. To overcome this situation, the duty cycle of the output time series was reduced by one half before adding the two phase patterns. The resulting $\frac{1}{4}$ duty pattern is shown as the solid-line wave forms in the lower part of figure 2(*b*). The corresponding 2-D wave form shown for the full-duty harmonic frequency condition is shown as the dotted line. Here the 3-D wave intersections and reinforcing 2-D crossing give a kinematic sense of the triads set up by the mode forcing. In all cases, $\frac{1}{4}$ duty cycles were used for the 3-D inputs, and $\frac{1}{2}$ duty harmonic cycles were used for the 2-D inputs. Using this approach, other output series constructions were generated for the other wave-angle conditions.

4. Experimental procedures

4.1. *Mode frequencies and initial amplitudes*

The conditions for the experiment are summarized with respect to the neutral stability loop for the Blasius layer in figure 3. For the velocity of 6.2 m/s used throughout these investigations, the Reynolds number at the location of the heating wires, flow visualization smoke wire, and streamwise bounds within hot-wire surveys were made are shown in this figure. The lines of constant non-dimensional frequency ($F = 2\pi f\nu/U_\infty^2$) for plane TS modes used in the respective cases listed at the top are shown as the dotted ($F = 88$) and dashed ($F = 79$) lines.

Only oblique modes that had a streamwise frequency that was the subharmonic of the input TS mode were investigated here. Non-harmonic combinations have been investigated by Dal-Ferro (1987) and Corke & Dal-Ferro (1987). For the non-dimensional subharmonic frequency, $F = 39.5$, two cases with oblique wave angles at $\pm 45°$ and $\pm 59°$ were studied. These have been designated 90P and 150P because they required phase shifts between heating wires of 90° and 150°, respectively. A third case, at a different streamwise subharmonic frequency, $F = 44$, used a phase shift of 180° to produce wave angles at $\pm 61°$. The steeper wave cases were expected to be near the most amplified conditions given by Herbert (1983*b*).

The initial amplitudes were chosen to meet three criteria. The first was that the levels of two- and three-dimensional mode inputs be sufficiently large to overcome

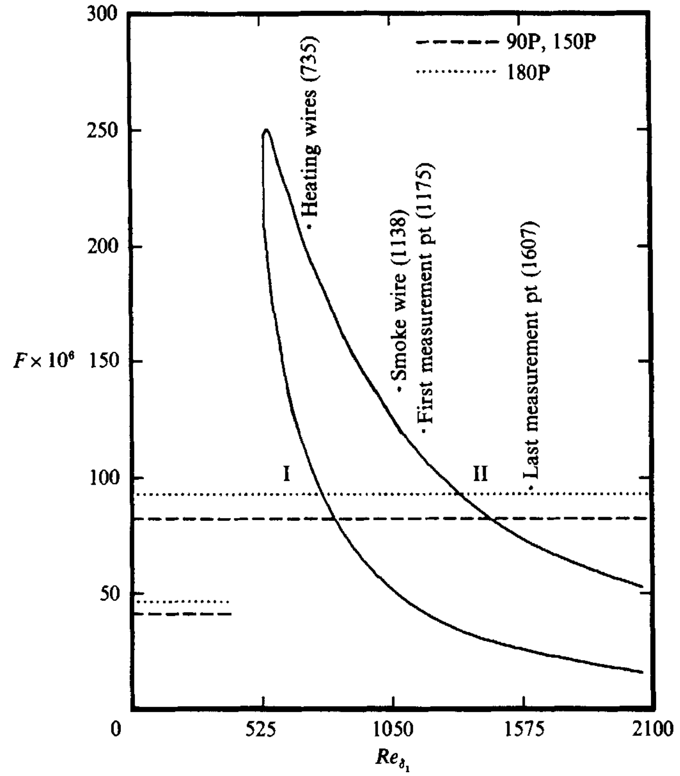

FIGURE 3. Positions of heating wires, smoke wire and measurement stations with respect to Blasius neutral curve for experimental conditions.

background levels. The second was that the location of enhanced growth of the subharmonic mode occur approximately midway down the test section, so as to allow a sufficient fetch for documenting a range of both linear and nonlinear development. The last criterion was that in at least one case the energy in the subharmonic mode should reach saturation limit and, past that point, transition to turbulence should occur. This last criterion was only met for the 150P case. For the other two, the choice of their streamwise and spanwise wavenumbers meant that one, 180P, just reached subharmonic saturation by the end of the test section, and the other, 90P, did not. The slower growth for these cases allowed a larger linear and weakly nonlinear range where more detailed surveys of the more slowly evolving instabilities could be performed.

The streamwise development and location of energy saturation were controllable through combinations of 2-D and 3-D initial amplitudes. We chose to fix the amplitude of one, the 3-D subharmonic, and to adjust the other to satisfy the above criteria. The initial amplitude of the 3-D mode was primarily determined to be the minimum amount needed to overcome the background disturbances. Since one of the objectives of the work was to investigate differences between the Craik (1971) and Herbert (1983*b*) mechanisms, we further constrained the level of plane wave (TS) forcing to be below the threshold value given by Saric & Thomas (1983) of 0.3% u'/U_∞ at Branch II of the neutral stability curve. This level of plane wave forcing was approximately four times lower than that used by Kachanov & Levchenko

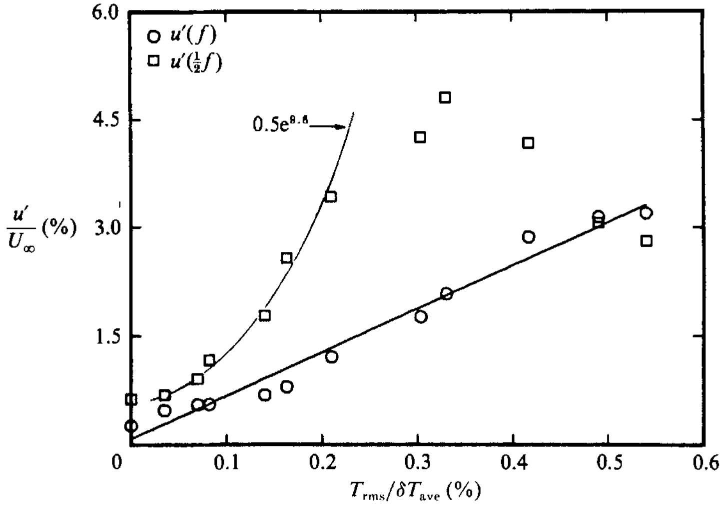

FIGURE 4. The effect of the subharmonic mode amplitude at $x = 152.5$ cm on the initial amplitude of the fundamental (plane TS) mode for 150P condition.

Case	Forcing frequency (Hz)	Phase shift (degrees)	Temperature perturbation Individual (Volts $T'/\delta T$)	Temperature perturbation Summed ($T'/\delta T$)
2D	32	—	45 0.33 %	0.33 %
90P	32	—	45 0.33 %	0.33 %
	16	90	2 0.31 %	0.36 %
150P	32	—	45 0.33 %	0.43 %
	16	150	1.75 0.31 %	0.29 %
180P	36	—	50 0.33 %	0.41 %
	18	180	2.25 0.31 %	0.24 %

TABLE 1. Initial temperature fluctuation levels due to mode seeding (2-D wire resistance = 45 ohms, 3-D wire resistance = 3 ohms, $\delta T = 7$ °C).

(1984). The ability to use such low levels of plane wave inputs was primarily a result of the controlled 3-D mode input provided by this experiment.

The effect of forcing levels on the resonant growth of the subharmonic is depicted in figure 4 for the case designated 150P. Shown in that figure are the normalized amplitudes of maximum streamwise velocity fluctuations of seeded fundamental (F) and subharmonic ($\frac{1}{2}F$) modes, measured at a fixed x-position 152.5 cm downstream of the heating wires. The quantity on the abscissa is the normalized r.m.s. temperature fluctuation which was measured with the miniature temperature sensor placed in the wakes of the heating wires, 3 mm downstream of the centre 3-D segment. δT is a local mean increase in air temperature due to the unsteady heating. The temperature perturbation in figure 4 is for the fundamental mode alone. This level was varied to see the effect on the growth of the oblique subharmonic mode. The level of forcing of the oblique mode was held fixed at the value given in table 1.

Focusing on the fundamental mode, we observe an approximately linear dependence of the maximum u'/U_∞ levels with temperature perturbation input. For

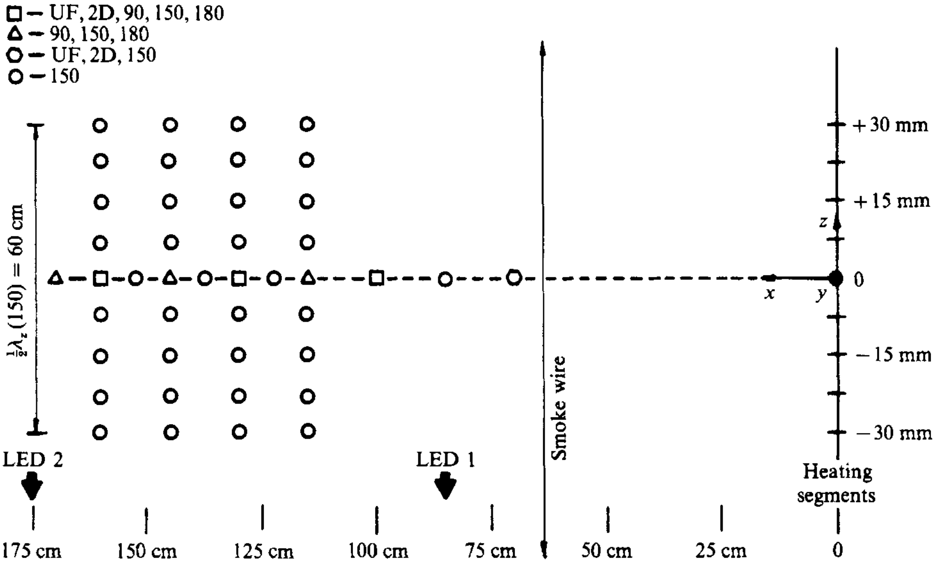

FIGURE 5. Laboratory coordinates and measurement locations for different experimental conditions.

the subharmonic mode, when the initial TS temperature perturbation is below approximately 0.05%, we observe little effect. Past that initial level, we observe an exponential increase in the amplitude of the subharmonic with increasing initial TS mode input. The growth eventually saturates, with a maximum fluctuation level of approximately 5% u'/U_∞, occurring at a temperature perturbation level of 0.33%. Increasing the initial TS mode amplitude beyond this point causes transition to turbulence to occur at this x-location with the resulting decay in subharmonic mode energy seen in the figure. Exercises such as this lead to the selection of initial temperature perturbation inputs to 2-D and 3-D modes summarized in table 1.

4.2. *Time-series acquisition*

Data time series were taken in 3-D space in the form of y-profiles for different streamwise, x, and spanwise, z, locations. The (x, z)-locations where profile data were taken are shown in figure 5. The x-coordinate in that figure is referenced to the position of the heating segments. The virtual origin of the Blasius layer was determined to be 45 cm upstream of the heating wires. In all cases except 150P, the measurements were restricted to the test section centreline, $z = 0$, which coincided with a point of intersection of the equal–opposite angled oblique modes, and a fluctuation amplitude maxima. For the 150P case, spanwise positions (seen as circles) were investigated at four x-locations. The total spanwise extent of those surveys covered one half of the spanwise wavelength of the subharmonic mode, which corresponds to three halves of the subharmonic lambda structure formed.

At every (x, z)-location, time series were taken at 20 different y-positions. For the dual sensor probes, this consisted of 16 records of 512 time-series voltage pairs, plus a voltage proportional to the y-position of the sensors. The y-positions were not equally spaced but grouped roughly according to equal mean velocity increments. At any given y-position, the computer would first sample the time series so as to maximize the gain (resolution) to the A/D converter. With the appropriate gain setting, a record of time-series points would be acquired and stored as raw voltage

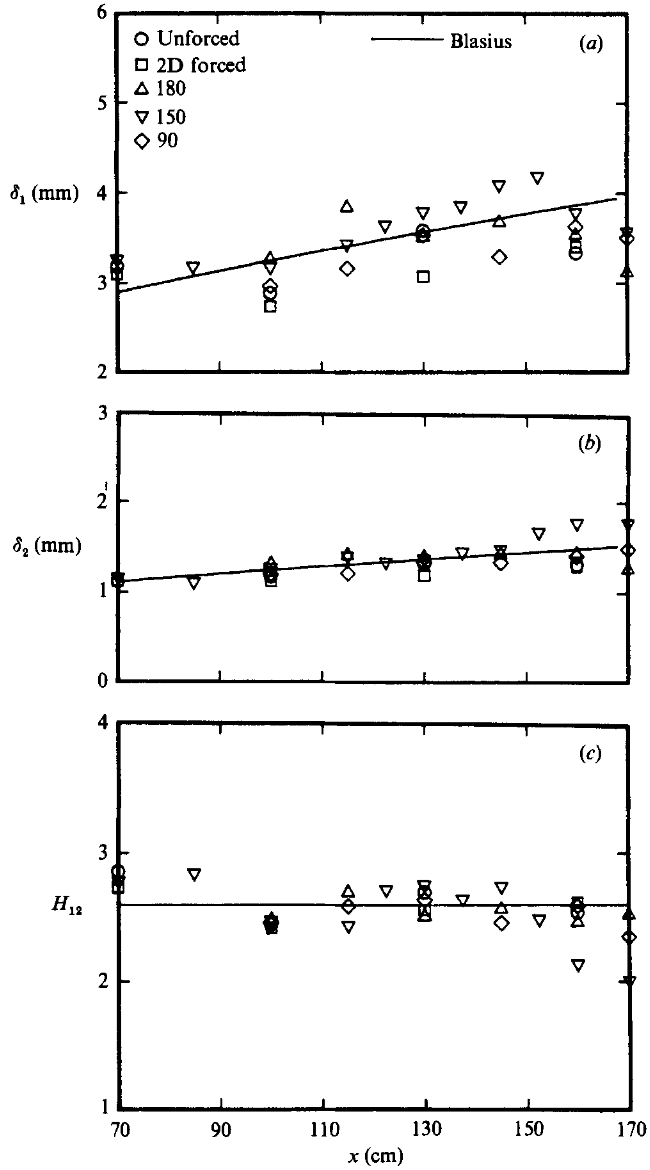

FIGURE 6. Streamwise growth of displacement (*a*) and momentum (*b*) thicknesses and shape factor (*c*) for all cases examined, with comparison to Blasius profile.

values on digital magnetic media. The storage required the mode forcing cycle to be interrupted. Therefore, prior to taking the next record of time-series points, the mode forcing was initiated and a 3 s delay was allowed before taking voltage samples to ensure that any start-up transients had convected past the measurement field.

4.3. *Processing techniques*

Linearization of the stored anemometer voltages was performed using a third-order polynomial with best-fit coefficients determined during sensor calibration runs. Typical calibration uncertainty was ± 0.01 m/s. The time-series velocity pairs were then summed and differenced to give the respective U and v or w component values.

To account for the growth of the boundary layer, a number of similarity quantities were computed and used to normalize the profile y-coordinate. These included the displacement thickness, δ_1, momentum thickness, δ_2, the ratio of these, H_{12}, and the Blasius variable $\eta = y(U_\infty/\nu x)^{\frac{1}{2}}$. The displacement and momentum thicknesses were determined by integrating the mean profile. The streamwise development of these are shown in figure 6. The comparison to the Blasius profile is also shown. For this, the Blasius virtual origin was found by the method of Bar-Sever (1984) and Corke *et al.* (1986). This involved finding, for a given mean velocity profile, the x-distance that minimized the squared error between it and Blasius. Analysis of all the profiles taken on the test section centreline for all the experimental conditions, forced and unforced, gave a consistent virtual origin at $x = -45$ cm (45 cm upstream of the heating segments).

In these calculations, the largest errors came from the determination of the probe position from the wall. This was done by fitting a straight line to the lowest portion ($\bar{U}/U_\infty < 0.40$) of each mean profile. This generally involved three points. The linear function was then used to extrapolate the profile to $U = 0$ which was enforced to be $y = 0$. The offset value was used to correct all of the y-positions of points in the profile. The mean profiles were derived from the Uw-sensor which, near the wall, was accurate to $\pm 2\%$. This produced an uncertainty in the wall extrapolation and thereby y-position which could translate into a 14% error in δ_1, a 5% error in δ_2 and an 8% error in H_{12}. Within these uncertainties, the comparison is acceptable.

The eigenfunction modulus and phase distributions for the natural, forced and interacted modes was determined from computations of frequency spectra of the velocity time series at each spatial location. In order to compute the phase development, the cross-spectra were determined. In each of the forced mode cases, the time series used to provide a phase reference were those taken closest to the wall, near the energy maxima for fundamental and subharmonic modes, on the centreline at the $x = 100$ cm locations (see figure 5). It was possible to use time-series information taken at a different time to provide a phase reference because the mode forcing and data acquisition were all phase locked by the control software.

Since the data series were acquired in phase with the mode forcing, with 24 samples per subharmonic cycle, phase-averaged velocity series were easily obtained. Typically 160 cycle averages formed from the sixteen 512-point data records was used. These phase-averaged time series formed the basic set used for calculations of velocity stream function and vorticity. Full details of those calculations are given by Mangano (1987).

5. Results – natural and 2-D seeded modes

5.1. *Unforced conditions*

The response of the basic flow to natural (unforced) disturbances is documented here. Profiles of the mean and total fluctuating velocity at four downstream positions are presented in figure 7. For the mean profiles the two sets of data at each x-position were derived separately from the uv- or uw-sensors. These show a good degree of repeatability and collapse to Blasius. Even though they represent all modes, the y-distribution of total streamwise velocity fluctuations have a shape which is characteristic of the TS eigenfunction modulus. Representative time traces of u-fluctuations at the height of the critical layer are shown at two x-positions in figure 8. These show a periodic character with amplitude which is growing with downstream distance.

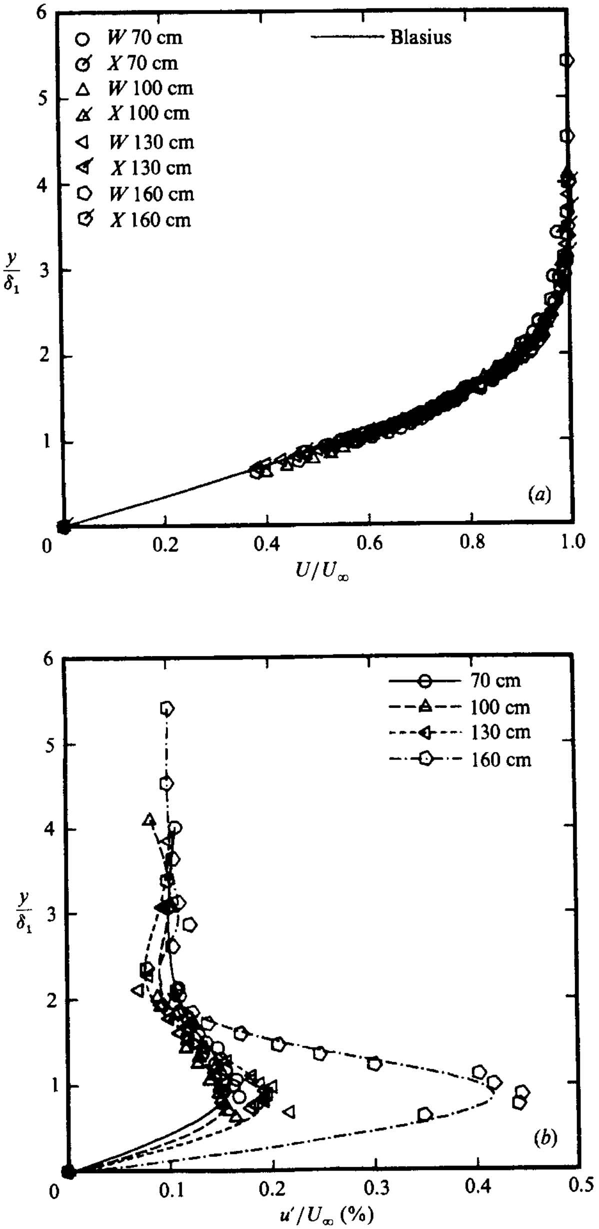

FIGURE 7. Normalized mean velocity profiles determined from *uv* and *uw* velocity probes (*a*) and total streamwise velocity fluctuations (*b*) at different downstream stations for unforced condition.

The y-distribution of frequency spectra for the three velocity components at the most downstream location in this set is shown in figure 9. These document a band of frequency centred at approximately 26 Hz ($F = 64$). This compares well with the most amplified TS frequency of 25 Hz obtained from linear theory for a Blasius boundary layer for the conditions at $x = 130$ cm ($Re_{\delta_1} = 1460$). The y-distribution of energy in this band in all three components is unmistakeably TS-like. Of course the broad-band nature is expected owing to the natural, random character of free-stream disturbances. In these cases, the flow remains laminar over the full length of the test

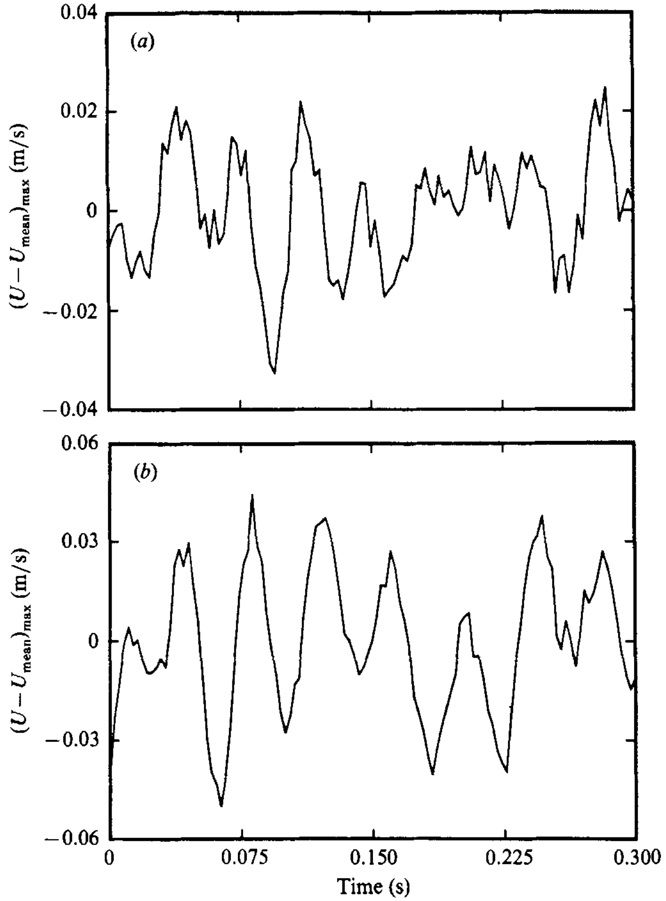

FIGURE 8. Representative time traces of maximum streamwise velocity fluctuations at (*a*) $x = 130$ and (*b*) 160 cm for unforced condition.

section, and there is no indication of other bands of frequencies, outside the most amplified TS band such as subharmonic or other harmonically interacted modes, appearing in the spectra.

5.2. *Two-dimensional forced modes*

The effect of the addition of coherent plane-wave modes into the base state previously documented is shown in the next four figures. The frequency of this mode was 32 Hz ($F = 79$, $\alpha\delta_1 = 0.25$), which was the same as used for the plane TS mode in the 90P and 150P resonance cases. This frequency falls within the band of most amplified modes previously documented to occur in the natural (unforced) boundary layer (figure 9). For consistency, the initial amplitude of this plane wave was set to be the same as for the 90P and 150P cases so that these results could also offer a direct comparison to those where oblique mode forcing was added to promote subharmonic resonance. These amplitude levels were listed in table 1.

Representative time traces at two x-positions upstream and downstream of Branch II (see figure 3) are shown in figure 10. These were taken at the height of the critical layer where the maximum amplitudes occur. At the upstream position, a regular periodic mode is documented. The peak-to-peak amplitude is approximately

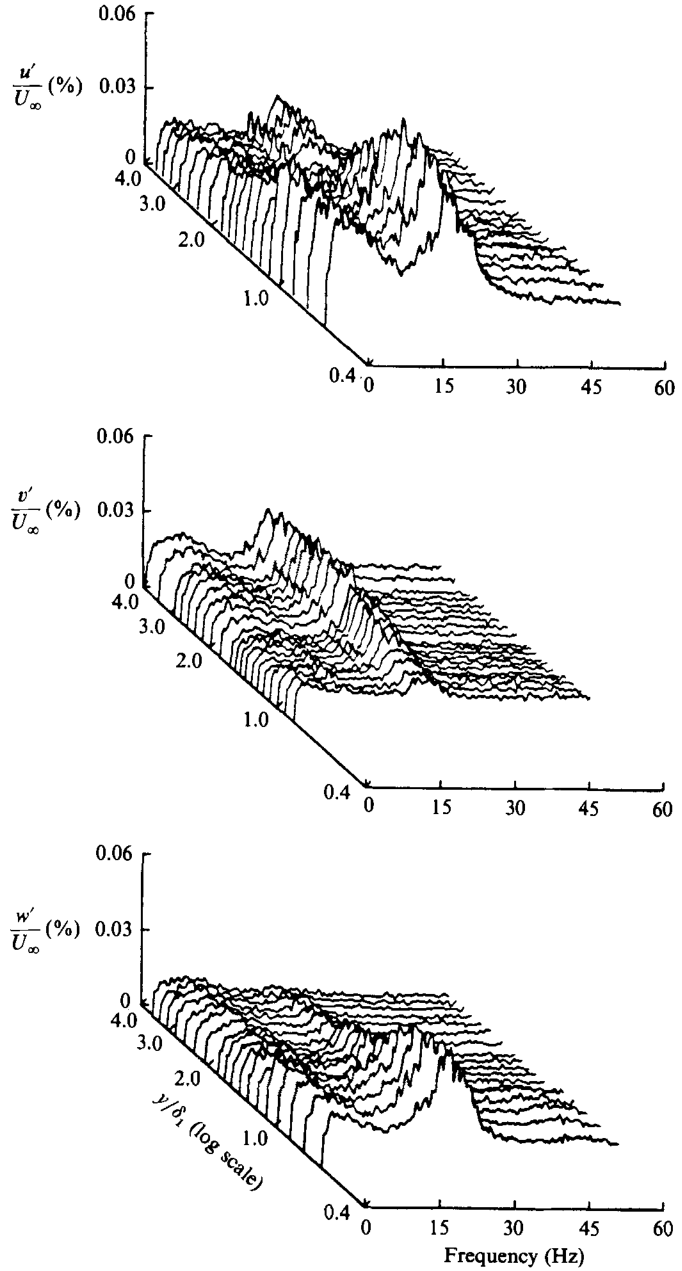

FIGURE 9. Normalized y-distribution of frequency spectra of three velocity components at $x =$ 160 cm for unforced condition.

equal to that of the unforced condition measured 60 cm further downstream ($x =$ 160 cm in figure 7). Further downstream this mode has amplified. In addition, there is some indication of an irregular subharmonic mode interspersed in the time trace.

We gain further insight into these modes from velocity spectra such as shown in figures 11–13. At the upstream position, the input 32 Hz mode is well defined by a sharp spectral peak. The y-distributions of u and v velocity components are characteristic of a plane TS-mode eigenfunction modulus. The appearance of a peak

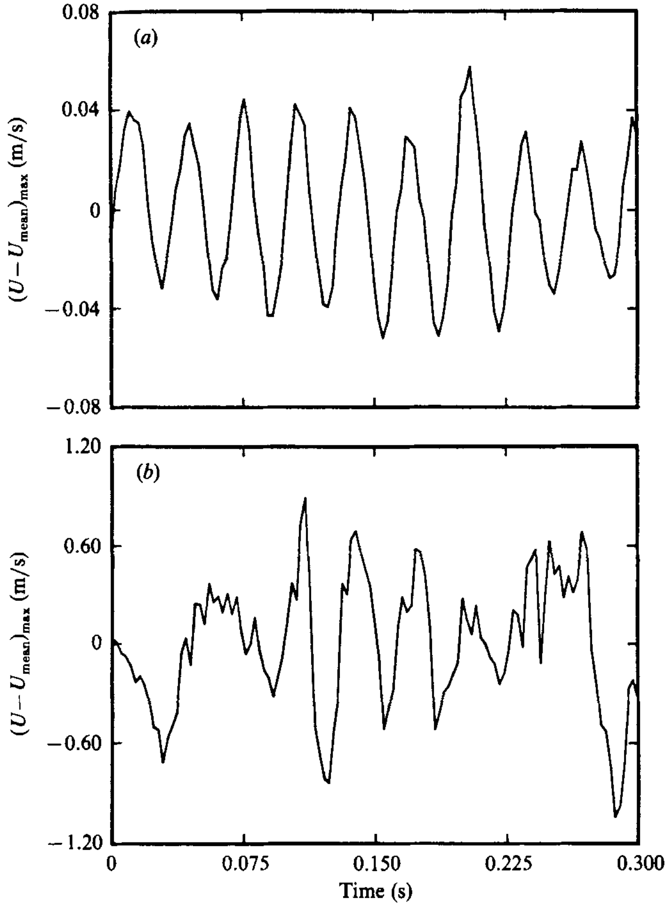

FIGURE 10. Representative time traces of maximum streamwise velocity fluctuations at (a) $x = 100$ and (b) 160 cm for 2-D seeded only condition.

in the w-component spectra suggests that a small amount of energy went into 3-D modes at this streamwise frequency. At an intermediate downstream position, $x = 130$ cm in figure 12, these modes have remained coherent and have amplified. The appearance of a small peak in the spectra at the subharmonic frequency is now evident in the streamwise velocity fluctuations. Since this subharmonic is partly a result of stochastic input it is not expected to be regular in space or time.

We have compared the growth rate of this mode at 32 Hz with linear theory for a Blasius layer. The experimental growth is based on the rate of increase of the maximum streamwise velocity fluctuations at increasing x-positions taken from spectra such as presented here. These yield a dimensional amplification rate, $-A_i\,\delta_1 = -0.0070$. At an intermediate Reynolds number, $Re_{\delta_1} = 1460$, and non-dimensional frequency $2\pi f\delta_1/U_\infty = 0.114$, linear theory predicts a maximum dimensionless amplification rate of approximately -0.0075 which is in close agreement.

At the last downstream position, $x = 160$ cm in figure 13, a quite broad-band energy distribution is evident in all three velocity components. Evidence of the initial TS frequency as well as a subharmonic still exist, but there is a generally larger

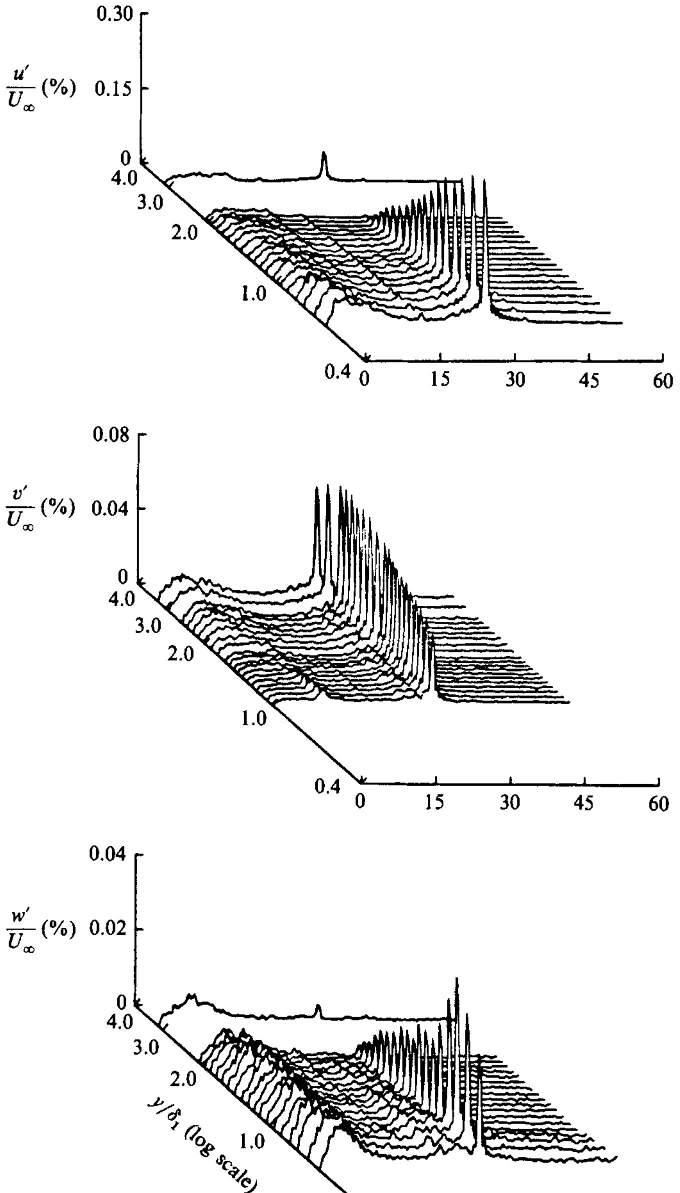

FIGURE 11. Normalized y-distribution of frequency spectra of three velocity components at $x = 100$ cm for 2-D seeded only condition.

base fluctuation level compared to the upstream position. At this x-station, the mean profile is still Blasius, and the total maximum r.m.s. streamwise fluctuation amplitude is 6 % of the free-stream velocity. Of this fluctuation total, 1.0 % is at the fundamental frequency and 0.6 % is at the subharmonic frequency.

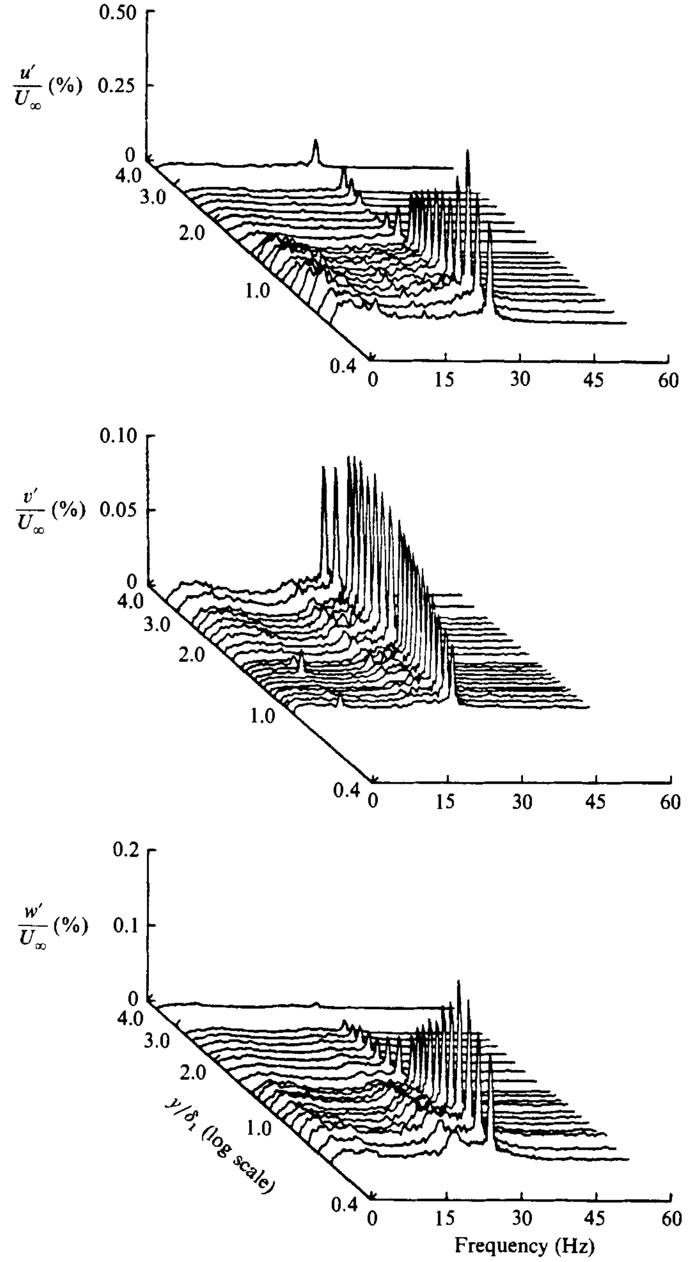

FIGURE 12. Normalized y-distribution of frequency spectra of three velocity components at $x = 130$ cm for 2-D seeded only condition.

6. Results – resonance conditions

6.1. *Results from flow visualization*

The flow visualization records in figure 14 document the basic state of the flow without any mode forcing (*a*), when forcing only oblique waves with wave angles of ±61° (180P), dimensionless wave numbers of (0.150, 0.281) (*b*), and (*c*) with the

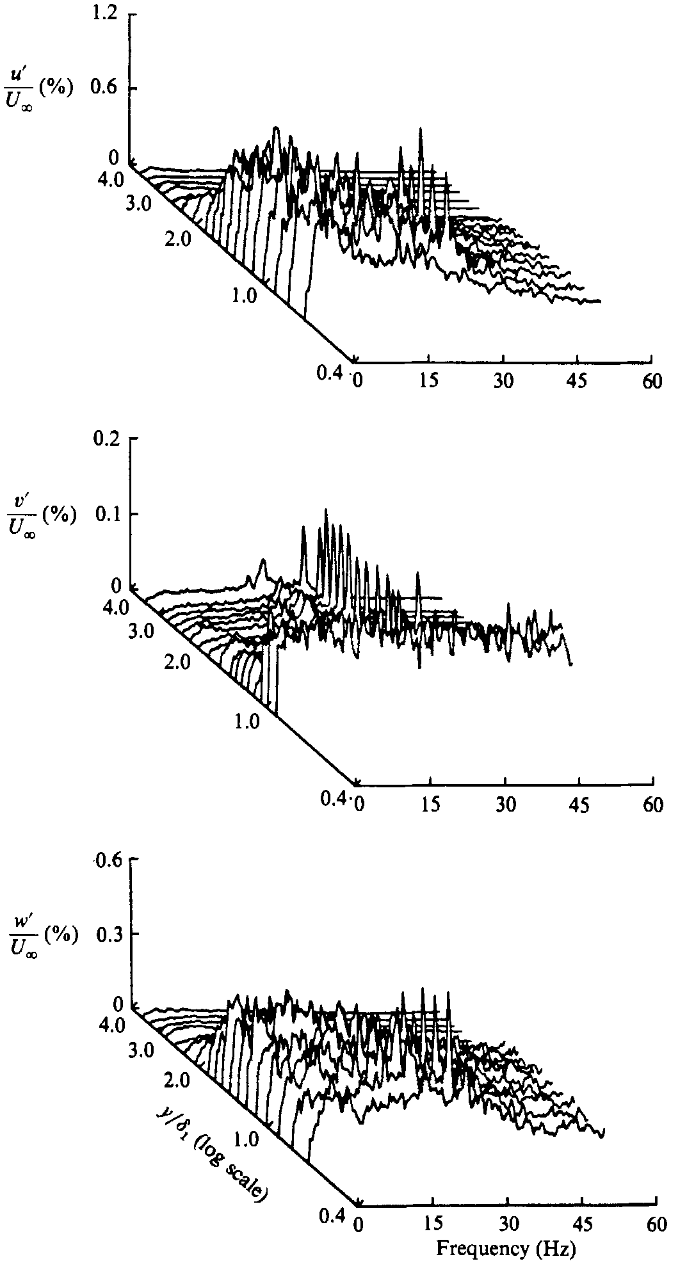

FIGURE 13. Normalized y-distribution of frequency spectra of three velocity components at $x = 160$ cm for 2-D seeded only condition.

combined forcing of the oblique wave condition of the middle photograph and forced plane TS waves at the harmonic wavenumber (0.300, 0). The field of view spans the full width of the measurement section and encompasses a region from 85 to 175 cm downstream of the heating segments as marked by the point lights at the bottom (see also figure 5). At the upstream edge of the photographs, $Re_{\delta_1} = 1250$.

Figure 14(a) documents the existence of plane TS waves which travel the length

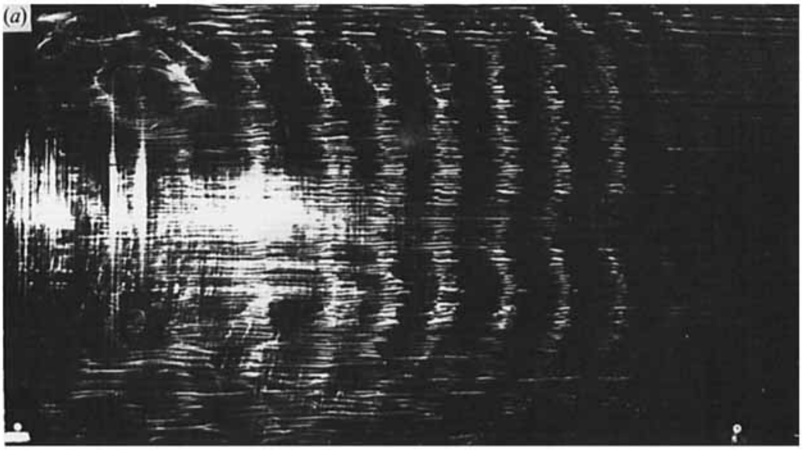

x = 175 cm Unforced 85 cm

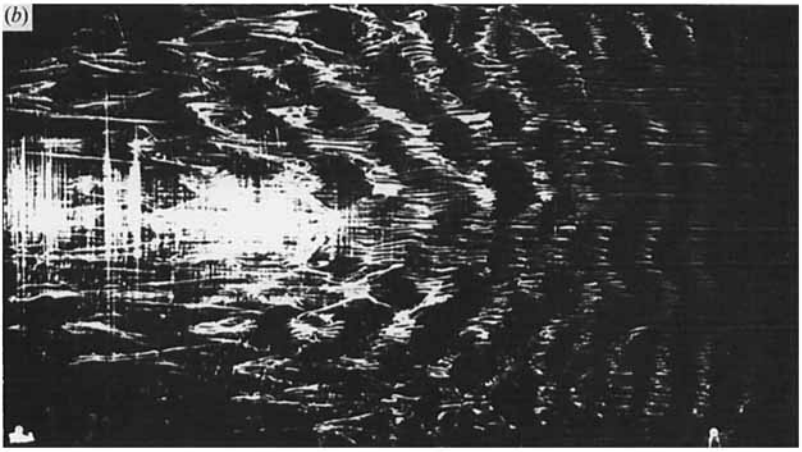

Oblique forcing (18 Hz)

Oblique plane forcing (18/36 Hz)

FIGURE 14. Visualization records documenting (*a*) natural unseeded, (*b*) seeded oblique wave alone and (*c*) seeded resonance conditions.

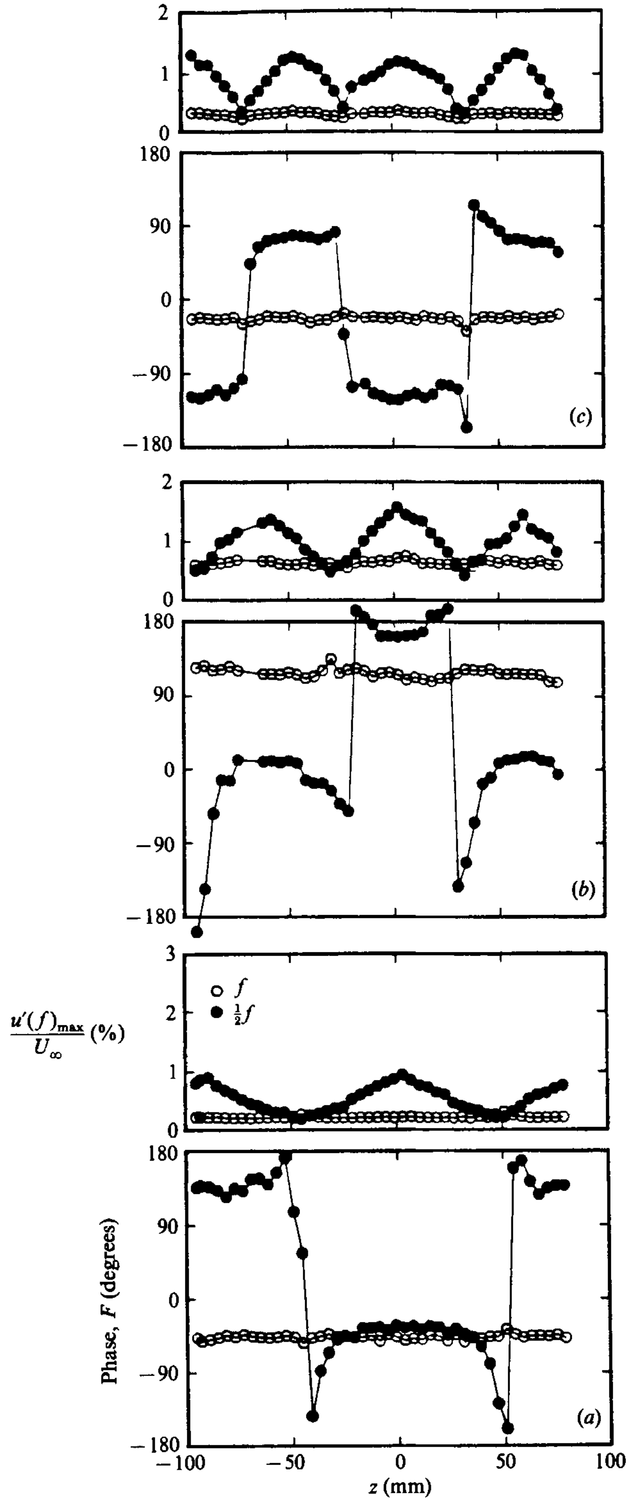

FIGURE 15. Spanwise distribution of maximum streamwise velocity fluctuations and phase for fundamental (plane TS) and subharmonic (oblique) modes for (*a*) 90P at $x = 150$ cm, (*b*) 150$\bar{\text{P}}$ at $x = 130$ cm and (*c*) 180P at $x = 130$ cm.

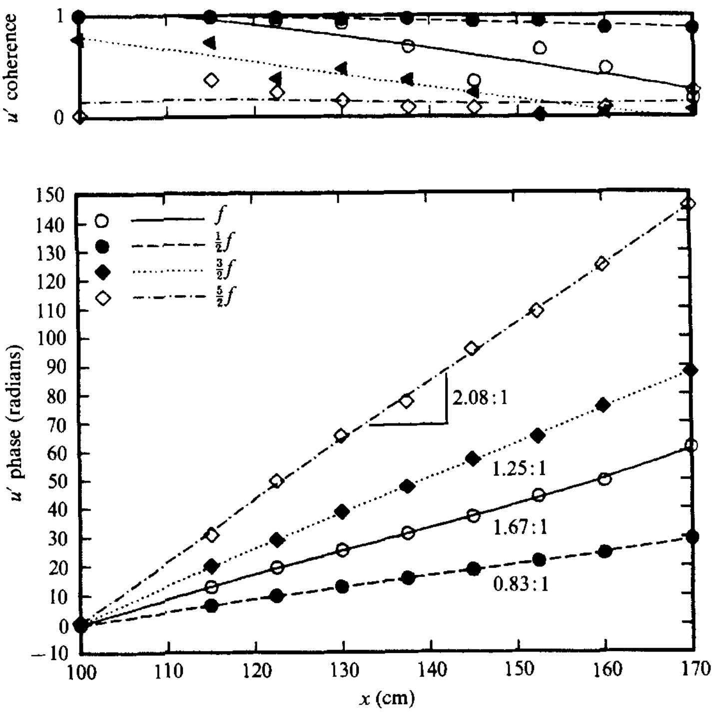

FIGURE 16. Streamwise variation of phase and linear coherence of f, $\frac{1}{2}f$, $\frac{3}{2}f$ and $\frac{5}{2}f$ modes for 150P condition.

of the test section in the unforced condition. These correspond to the periodic velocity field and energy distributions seen in figures 7(*b*), 8 and 9. The naturally growing modes are weak and easily overcome with mild seeding of oblique waves whose effect is shown visually in figure 14(*b*). With the addition of the seeded plane waves at twice the streamwise wavenumber of the oblique waves, the flow is seen to develop a spanwise array of lambda vortex patterns which ultimately stretch and break down to turbulence. The streamwise location where the lambda patterns first emerge is related to the initial amplitudes of the plane and oblique wave combinations as well as the spanwise wavenumber of the oblique modes. As will be apparent from hot-wire measurements presented in later figures, the first emergence of the staggered lambda patterns marks the region of enhanced growth of energy at the subharmonic (oblique mode) frequency through a resonant interaction with the fundamental plane mode.

6.2. *Wavenumber determination*

The spanwise variation of magnitude and phase of streamwise velocity fluctuations in fundamental (open symbols) and subharmonic (closed symbols) modes is shown in figure 15 for the three resonance cases. The x-location for the 150P and 180P conditions is 130 cm downstream of the heating segments. For the less amplified 90P case, the x-position is slightly further downstream, at $x = 150$ cm, to give a comparison at subharmonic amplitudes comparable to the others. The spanwise measurements in these figures were taken at a fixed y, close to that of the critical layer, so that the fluctuation amplitudes surveyed are near their maximum at that x-position.

Focusing first on the least amplified, 90P case in figure 15(*a*), we observe a

Case	f_1 (Hz)	$f_{\frac{1}{2}}$ (Hz)	F_1 ($\times 10^6$)	$F_{\frac{1}{2}}$ ($\times 10^6$)	$\alpha_1 \delta_1$	$\alpha_{\frac{1}{2}} \delta_1$
90P	32	16	79	39.5	0.250	0.125
150P	32	16	79	39.5	0.250	0.125
180P	36	18	88	44	0.300	0.166
150PC	32	16	79	39.5	0.250	0.125
180PC†	36	18	88	44	0.300	0.150

Case	$\lambda_{z\frac{1}{2}}/\delta_1$	$\beta_{\frac{1}{2}} \delta_1$	θ (deg)	$(C_r/U_\infty)_1$	$(C_r/U_\infty)_{\frac{1}{2}}$
90P	59	0.106	40 (45)	0.38	0.38
150P	40	0.157	52 (59)	0.38	0.38
180P	30	0.212	52 (61)	0.36	0.36
150PC	31	0.205	59 (59)	0.38	0.38
180PC†	22	0.281	61 (61)	0.36	0.36

Case	$f_{\frac{3}{2}}$	$\alpha_{\frac{3}{2}} \delta_1$	$(C/U_\infty)_{\frac{3}{2}}$	$f_{\frac{5}{2}}$	$\alpha_{\frac{5}{2}} \delta_1$	$(C/U_\infty)_{\frac{5}{2}}$
150PC	48	0.377	0.38	80	0.605	0.38

$\delta_1 = 3.0$ mm at the most upstream measurement point where $Re_{\delta_1} = 1250$.
† Taken from Corke & Dal-Ferro (1987).

TABLE 2. Forced and dominant interactive modes.

spanwise-uniform amplitude and phase distribution for the fundamental mode which is consistent with a plane wave. The subharmonic mode is observed to have maxima and minima in fluctuation levels in span which is consistent with the seeded oblique wave intersections. The spanwise phase distributions document that the minima coincide with a 2π phase shift of that mode. The spanwise distance, λ_z, giving a 2π shift in phase (also twice the distance between adjacent minima) was used to calculate the spanwise wavenumber, $\beta = \pm 2\pi/\lambda_z$. This can be similarly derived from the flow visualization records, such as figure 14 for the 180P case, as the spanwise distance between structure valleys.

The spanwise distributions in the more amplified cases (figure 15*b*, *c*) show similar behaviour, with the appropriate reduced spanwise wavelength. One can begin to detect some slight spanwise variation in the fundamental mode amplitude which is the precursor of a nonlinear interaction with the subharmonic mode leading to a 3-D mode at the fundamental frequencies. This process will be discussed in great detail in a later section.

The values of streamwise wavenumber were determined by measuring the x-development of phase of the fundamental and subharmonic modes. A sample of these results, which also includes two interacted modes ($\frac{3}{2}f$ and $\frac{5}{2}f$), for the most amplified, 150P, case is shown in figure 16. Also shown at the top of the figure are the values of linear coherence. For these, the reference time series was taken at the streamwise position, $x = 100$ cm, at the same cross-stream position, $x = 0$ cm, and at the y-position of the subharmonic (and fundamental at this reference x) mode energy maximum. Based on these, the streamwise wavenumbers (slopes) and phase velocities, $C_r = 2\pi f/\alpha$, were calculated. All these modes have the same constant phase velocity, $C_r/U_\infty = 0.38$, which matches that of the plane TS mode, and therefore satisfies the criterion for resonance. The same was also true for the other resonance cases (90P and 180P) not shown here (Mangano 1987).

These results, which document the seeded wavenumber conditions, are compiled in table 2. In that table, the distinction 150PC corresponds to values obtained from

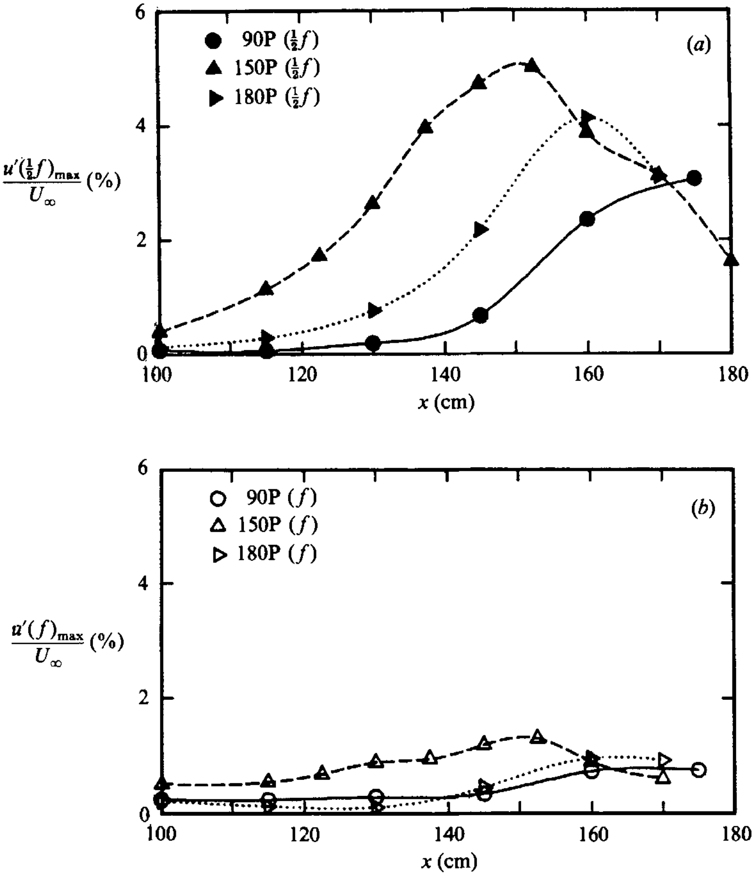

FIGURE 17. Downstream development of maximum streamwise velocity fluctuations in (b) fundamental and (a) subharmonic modes for 150P condition.

full eigenfunction profiles taken from time series acquired with the acquisition computer (C), rather than the other statistics which were acquired by hand as single spatial point values at a fixed y. The only difference that arises from these two approaches is in the determination of the spanwise wavenumber, β (and $\lambda = 2\pi/\beta$). As will be seen in later figures on the spanwise distribution of the subharmonic eigenfunction modulus, taking measurements in span at a fixed y set at the height of the centreline maximum, gives a slightly distorted measure of the spanwise energy distribution. The bracketed wave angles ($\theta = a\tan\beta/\alpha$) contain the expected values based on the input conditions. When determined from the full profile data taken off-centre, 150PC, these agreed well. Confirmation of the 180P case has come in off-centreline measurements by Corke & Dal-Ferro (1987) labelled 180PC in table 2.

6.3. *Centreline measurements*

The x-growth of the maximum streamwise velocity fluctuations in the fundamental and subharmonic modes are documented for the three resonance cases in figure 17. The 3-D subharmonic is shown at the top (a) in filled symbols and the fundamental at the bottom (b) in similar open symbols. These were measured while moving downstream along a constant $z = 0$ line which passes through oblique wave intersections, and subharmonic energy maxima of figure 15. From the point of initial

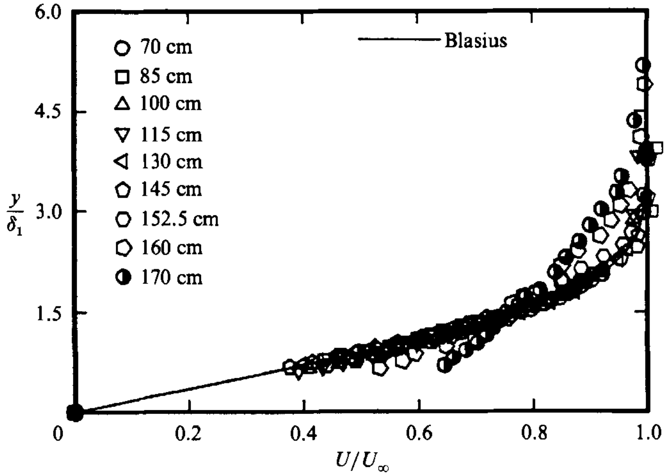

FIGURE 18. Downstream development of mean velocity profile on centerline ($z = 0$) for 150P condition.

seeding, the fundamental plane TS mode grows according to linear theory until it reaches Branch II ($x = 117$ cm for the 90P and 150P cases, $x = 95$ cm for the 180P case). By linear theory, the steep-angled subharmonic oblique waves are highly damped, and upstream of the TS Branch II, their amplitude is considerably lower than that of the fundamental. This is best observed in the slower growing 90P case where the amplitude of streamwise fluctuations in the subharmonic and fundamental modes at Branch II were 0.018% and 0.227%, respectively. In both the 150P and 180P cases, the initial amplitude of the fundamental mode was the same as for the 90P case. The higher amplitudes seen at Branch II are a result of an interaction with the faster growing subharmonic in the two cases in which the 3-D mode is more amplified.

For finite amplitudes of the fundamental, energy transfer occurs between it and the subharmonic. Once the subharmonic grows to a large enough amplitude, it can gain further energy from the mean flow. The subharmonic mode continues to grow until it saturates. Past saturation, the flow transitions to turbulence which is manifested in a loss of linear phase locking with an upstream reference, a broad-band velocity spectrum, and a deviation from the Blasius profile to a more full profile with a smaller displacement thickness, a larger momentum thickness, and thereby larger shape factor and viscous drag. Downstream changes in the mean profile are documented for the most amplified 150P case in figure 18.

Past Branch II, energy at the initial TS frequency is expected to decay with downstream distance. Once the energy in the subharmonic mode grows to a sufficient level, however, energy in the fundamental mode is observed to grow in accordance with the subharmonic. It will be documented later that this mode, at the fundamental frequency, is a new 3-D interacted mode with spanwise wavenumber $\pm 2\beta$.

For the same initial amplitudes, the rate that the subharmonic mode grows is dependent on its streamwise and spanwise wavenumbers. This effect is shown in figure 19, which documents the x-development of the local dimensional amplification rates of the subharmonic mode for the three curves in figure 17(*a*). The solid and dashed curves directly show the effect of changing spanwise wavenumber; $\beta\delta_1 =$ 0.106 and 0.205 respectively. Of the three, the dashed (150P) case is the most

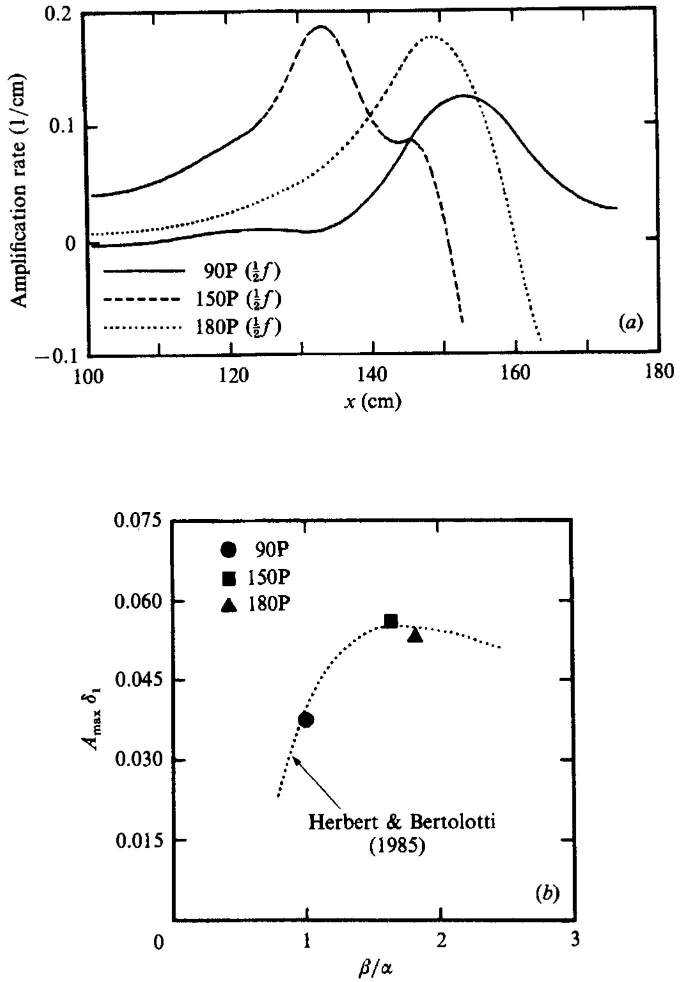

FIGURE 19. (*a*) Downstream development of subharmonic mode amplification rate for three resonance conditions, and (*b*) effect of maximum amplification on spanwise wavenumber.

amplified. The maximum amplification for the three cases is plotted versus their respective ratios of spanwise to streamwise wavenumbers in figure 19(*b*). Drawn for comparison is the theoretical dependence of spatial amplification determined by Bertolotti (1985) and Herbert & Bertolotti (1985), which was intended to model the experimental conditions of Kachanov & Levchenko (1984). In this presentation the curve had been shifted upward to place it in the region of amplification rates for the initial amplitudes and Reynolds numbers in our experiment. The dependence on the wavenumber ratio is in remarkable agreement.

The location of maximum subharmonic amplification roughly marks the first appearance of 3-D staggered peaks in the flow visualization records. For the 150P case, it occurs well upstream (approximately 20 cm, two subharmonic wavelengths) of the x-position of subharmonic energy saturation. The case with the same streamwise wavenumber (90P) is similar. For the dotted curve case (180P), the x-position of maximum amplification occurs further downstream and closely coincides with the point of energy saturation seen in figure 17. The close coincidence of these

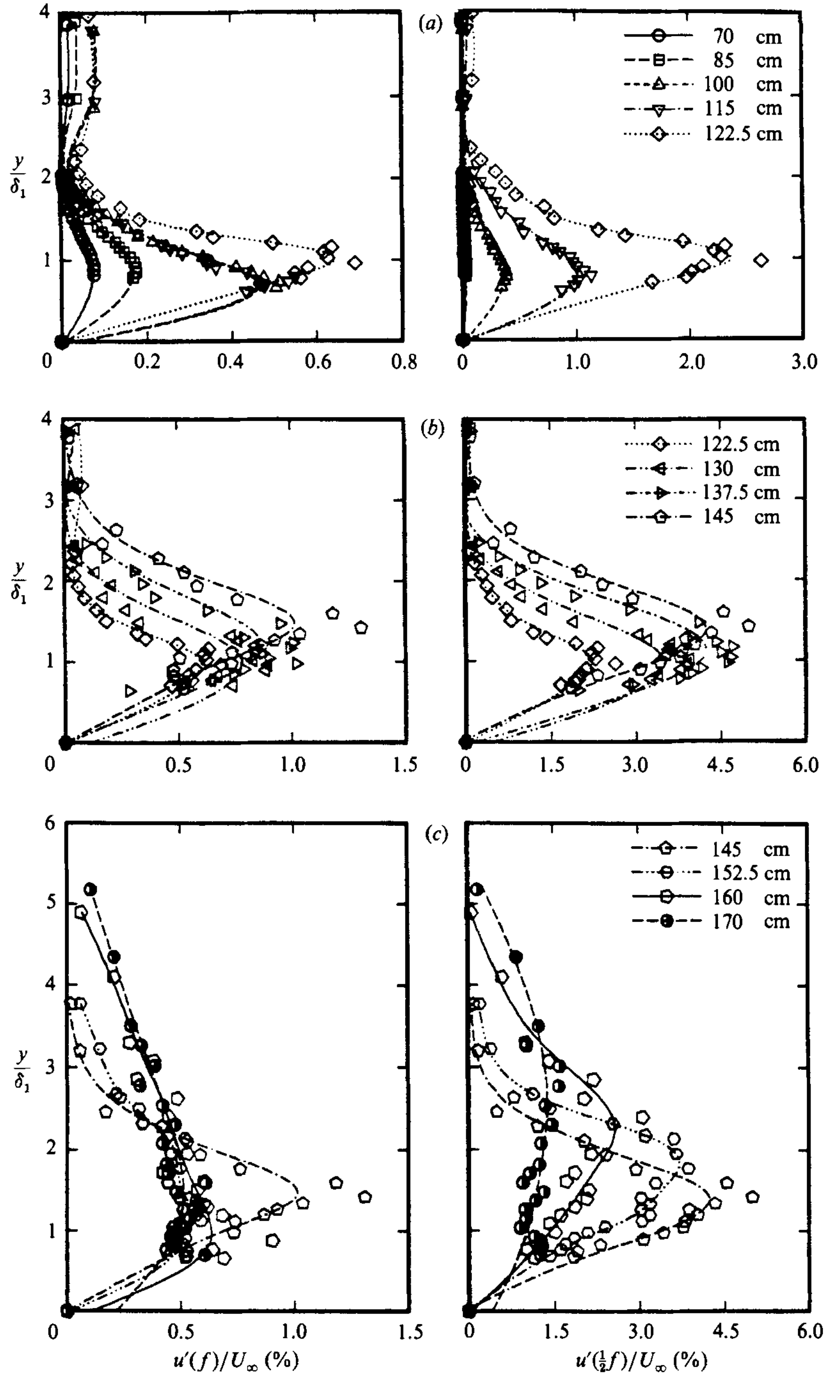

FIGURE 20. Vertical distribution of u-component velocity fluctuations in fundamental (left) and subharmonic (right) modes along $z = 0$ line at (*a*) $x = 70$–122 cm, (*b*) 122–145 cm, and (*c*) 145–170 cm for 150P condition.

two important points of development of the 180P subharmonic growth curve has been documented to produce extra strong nonlinear phase locking (Corke & Dal-Ferro 1987).

As the subharmonic mode develops, there are a number of characteristic changes which take place in the boundary layer. These can be seen by examining the eigenfunction modulus and phase distributions in figures 20 and 21. For these we focus on the most amplified (150P) condition. As can be seen from figure 20(*a*), the u-eigenfunctions moduli show little growth in the subharmonic mode (right) until $x = 100$ cm. For the fundamental mode (left), neutral growth is observed between $x = 100$ and 115 cm. The y-location of the eigenfunction maxima for both modes coincides with the height of the critical layer, $y/\delta_1 = 0.7$. The peak in the subharmonic distribution is relatively broad at this stage of development and therefore is considered to roughly coincide with the y-height of the peak of the fundamental. At this x-position (115 cm), the level of the subharmonic eigenfunction maximum is roughly twice that of the fundamental. By the next measurement station, $x = 122.5$ cm, a factor-of-two growth and the movement from the wall of the energy maximum of the subharmonic mode now signals the strong nonlinear development. The simultaneous large growth in the fundamental maximum and its movement from the wall indicates a tie to subharmonic development.

Up to and including the $x = 122.5$ cm position, the y-distribution of the u-eigenfunction phase of both the fundamental and subharmonic modes, in figure 21 (*a*), are similar to that of a TS mode. A little over one TS wavelength downstream, the y-phase distribution begins to change. This is fully established by $x = 137.5$ cm in figure 21 (*b*). In this case, it goes from the 'wave-like' TS distribution to a 'structure-like' distribution with the phase changing nearly linearly away from the wall. This distribution holds until the loss of linear phase coherence past energy saturation. We interpret this change in phase character to be an indication of the reorientation and stretching by the mean flow of the now-formed lambda structure. Off the structure centreline, at this point of development, the wave-like phase distribution still exists (Mangano 1987).

With increasing downstream distance, the maxima in the u-eigenfunctions of both modes continues to grow and move steadily from the wall. Beyond the point of subharmonic saturation, the subharmonic eigenfunction maximum decreases but the location continues to move away from the wall, even to the last examined x-location. Past saturation, the eigenfunction of the fundamental collapses to a self-similar distribution. The collapse appears to be a consistent precursor of full transition. At this stage there is little linear phase coherence with the fundamental mode (figure 16). The mean velocity profile, seen in figure 18, has changed from the Blasius distribution to the more full distribution of a turbulent layer. It has not yet appeared to reach self-similarity by the last station, however. The deviation of the mean profile at his stage is localized to the centreline of the lambda structure. On either side of this z-position, the mean profile is still Blasius (Mangano 1987). As such, the structure is essentially breaking down in an outward progression from its centreline.

The centreline x-development is further illustrated in the selected time series and component velocity spectra in figures 22 and 23. Upstream of Branch II at $x =$ 100 cm, the amplitudes of streamwise velocity fluctuations of the fundamental and subharmonic modes are nearly equal. Approximately two subharmonic TS wavelengths downstream (at $x = 115$ cm), the subharmonic mode has grown by a factor of two over the fundamental. Some very low-amplitude broad frequencies also begin to appear near the wall in the v- and w-component spectra. The amplitudes of

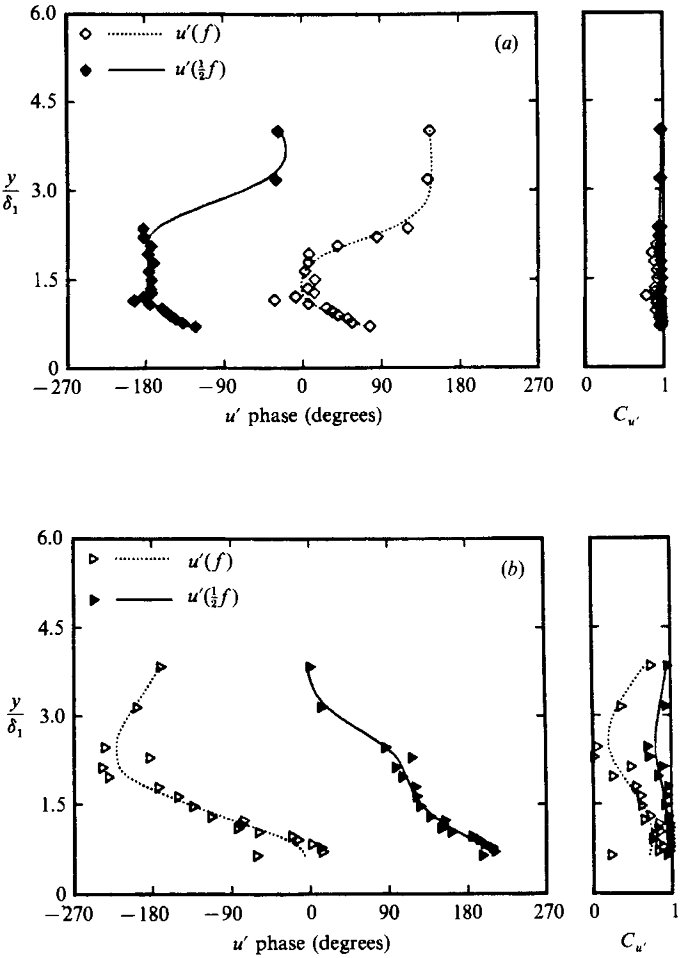

FIGURE 21. Vertical distribution of phase and linear coherence for fundamental and subharmonic modes along $z = 0$ line at (*a*) $x = 122$ and (*b*) 137 cm for 150P condition.

these broad-band components decrease away from the cross-stream centreline of the lambda structure (Mangano 1987).

The broad-band components which first appeared on the centreline in the v- and w-components near the wall have progressively spread away from the wall by $x =$ 145 cm (figure 23*c*). The u- and w-component spectra still show a dominant peak at the subharmonic frequency, which is still growing, being upstream of the point of energy saturation. Past the point of saturation at $x = 160$ cm (figure 23*d*) the broad frequencies now appear fully in the u-component spectra and time series. The subharmonic peak is still dominant although decreasing in magnitude. In this process, there was no indication of coherent higher frequency 'spike' stages as in the case of Klebanoff *et al.* (1962). Rather there appeared to be a smooth merging and filling of broad-band frequency components. In a later section we shall attempt to quantify this process which we feel is fundamental to the transition to turbulence involving two or more resonantly phase-locked modes.

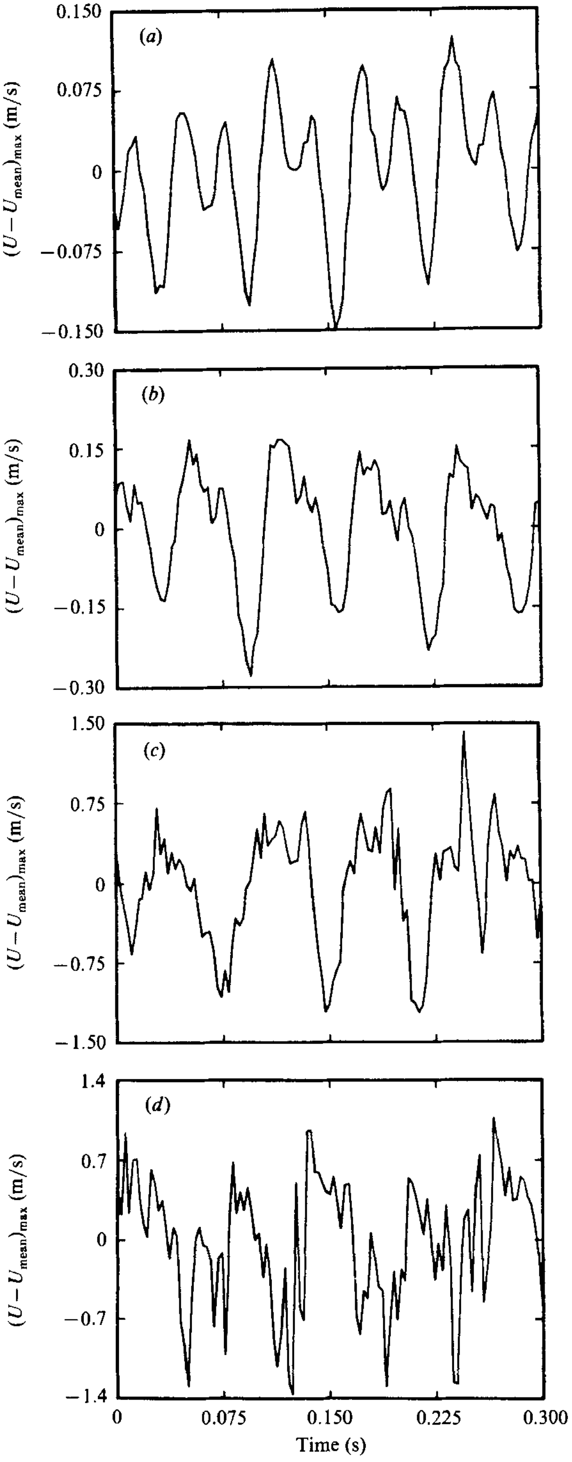

FIGURE 22. Representative time traces of maximum streamwise velocity fluctuations at (*a*) $x = 100$, (*b*) 115, (*c*) 145 and (*d*) 160 cm for 150P condition.

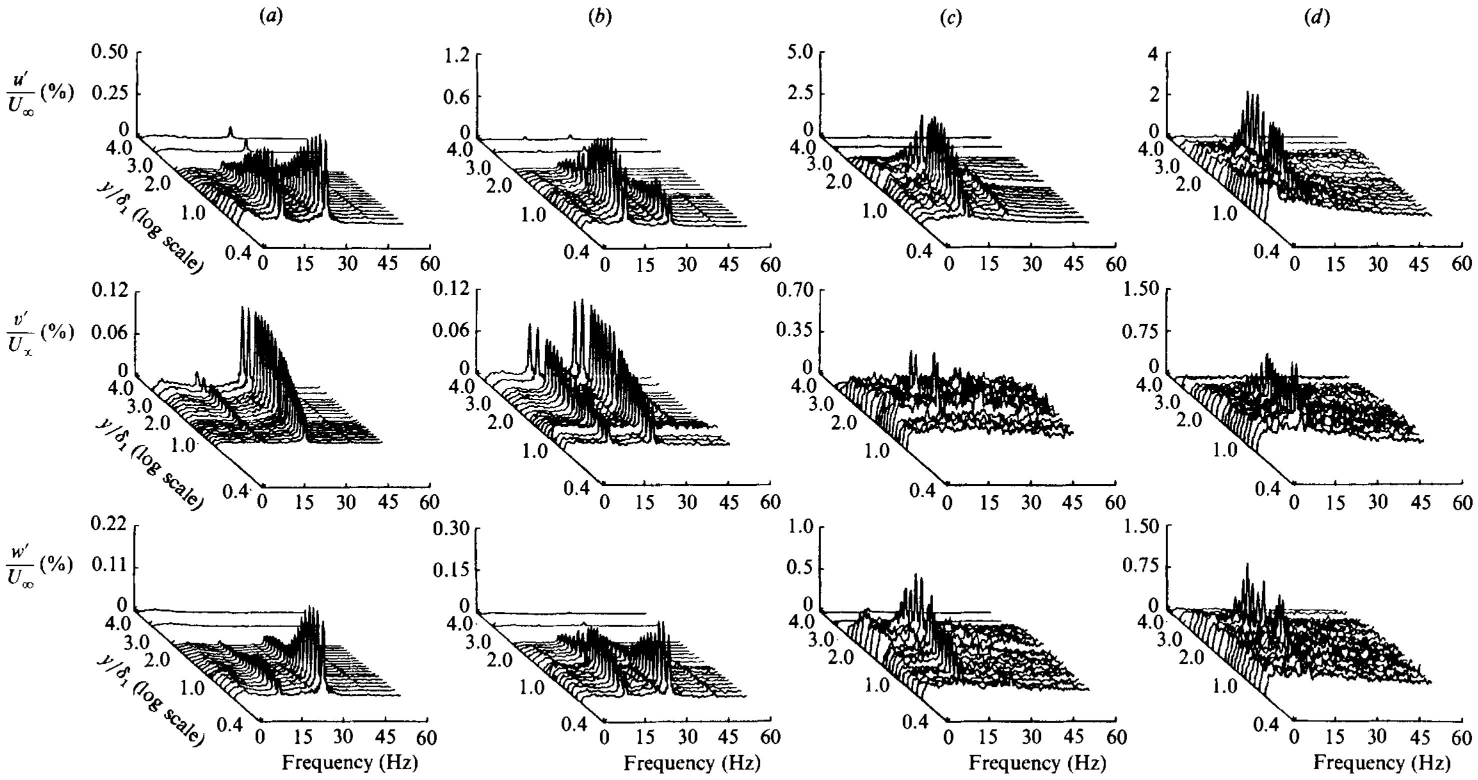

FIGURE 23. Normalized y-distribution of frequency spectra of three velocity components represented by time series of figure 22.

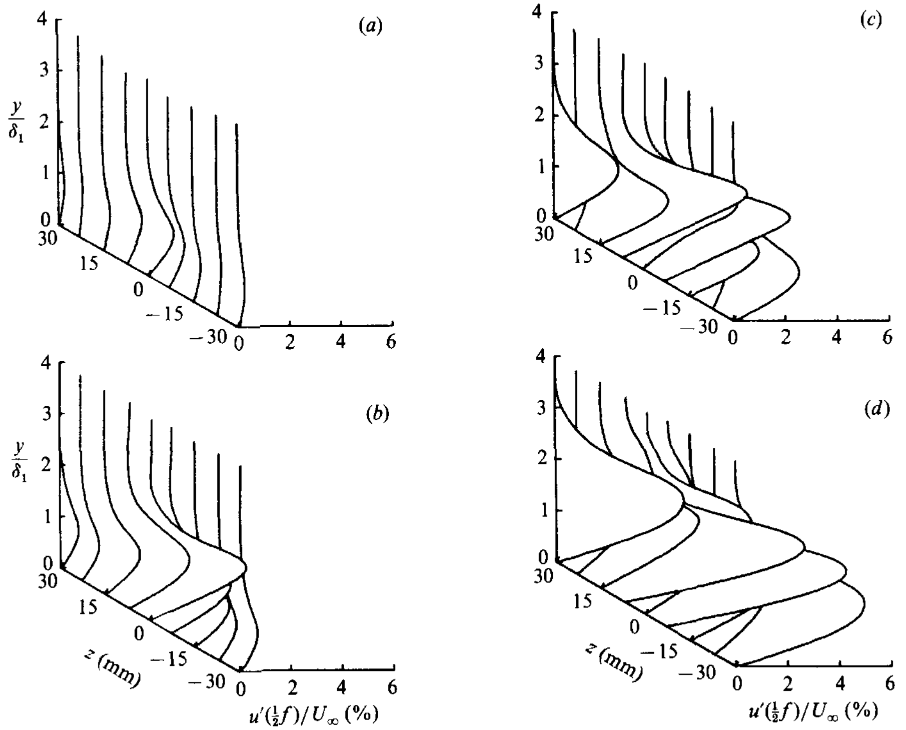

FIGURE 24. Spanwise distribution of subharmonic mode u-eigenfunction moduli at (a) $x = 115$, (b) 130, (c) 145 and (d) 160 cm for 150P condition.

6.4. *Off-centreline measurements*

Off-centreline measurements were performed for the 150P case at four x-positions of 115, 130, 145 and 160 cm downstream of the heating wires (figure 5). The first is just upstream of Branch II for the TS mode, and the last two are just upstream and downstream of the point of energy saturation. At the two upstream positions, the distribution of streamwise fluctuations in figure 24 gives a sense of the initial lambda-shaped structure. In these and similar figures, the distributions have been plotted in 3-D perspective and reflected about $z = 0$ to give a more physical view. At this x-position the maximum is at the cross-stream centreline. By the next x-position, the u-eigenfunction maxima have moved to just off-centre positions. On the centreline, the fluctuation maximum is moving away from the wall. Clear minima are now evident at $z = \pm 23$ mm. The distance between these was used in computing the spanwise wavenumber in table 2 denoted as 150PC. The corresponding eigenfunction phase seen in figure 27 documents a 'structure-like' stretched distribution at the centre with 'wave-like' character near the amplitude minima. The subharmonic structure holds this same basic spanwise character past energy saturation, although the centreline maximum continues to move away from the wall and the spanwise extent of the stretched y-distribution of phase distribution increases.

The v-fluctuations in figure 25 develop a maximum on the centreline, initially away from the wall at $x = 130$ cm. As the lambda structure develops, this centreline maximum moves towards the wall and intensifies so that, by $x = 160$ cm, it is the location of the maximum v-component fluctuations. In contrast, the maximum w-component fluctuations develop on the sides of the lambda structure, where the u-

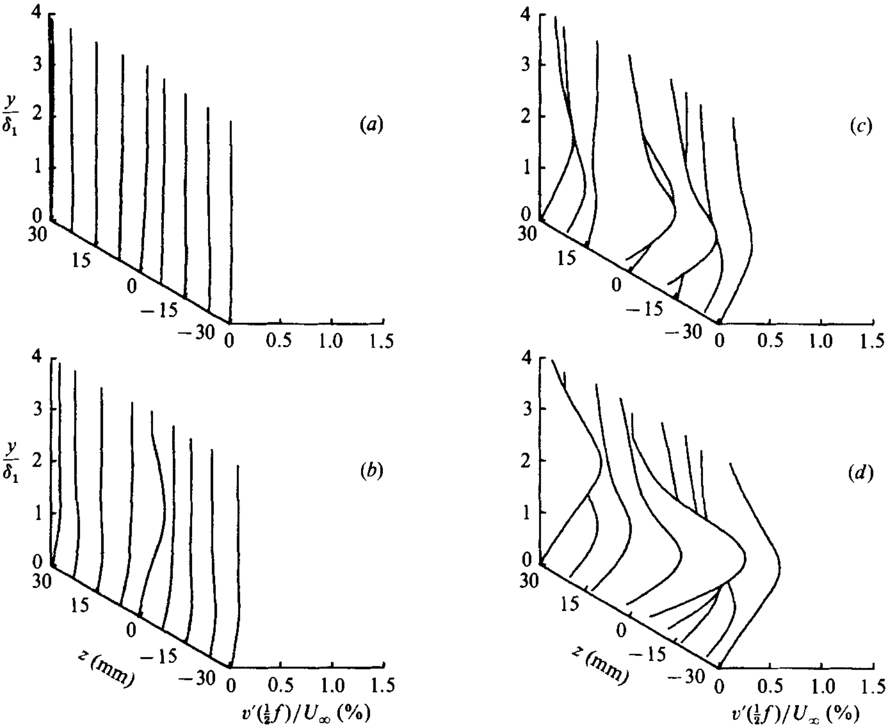

FIGURE 25. Spanwise distribution of subharmonic mode v-eigenfunction moduli at (a) $x = 115$, (b) 130, (c) 145 and (d) 160 cm for 150P condition.

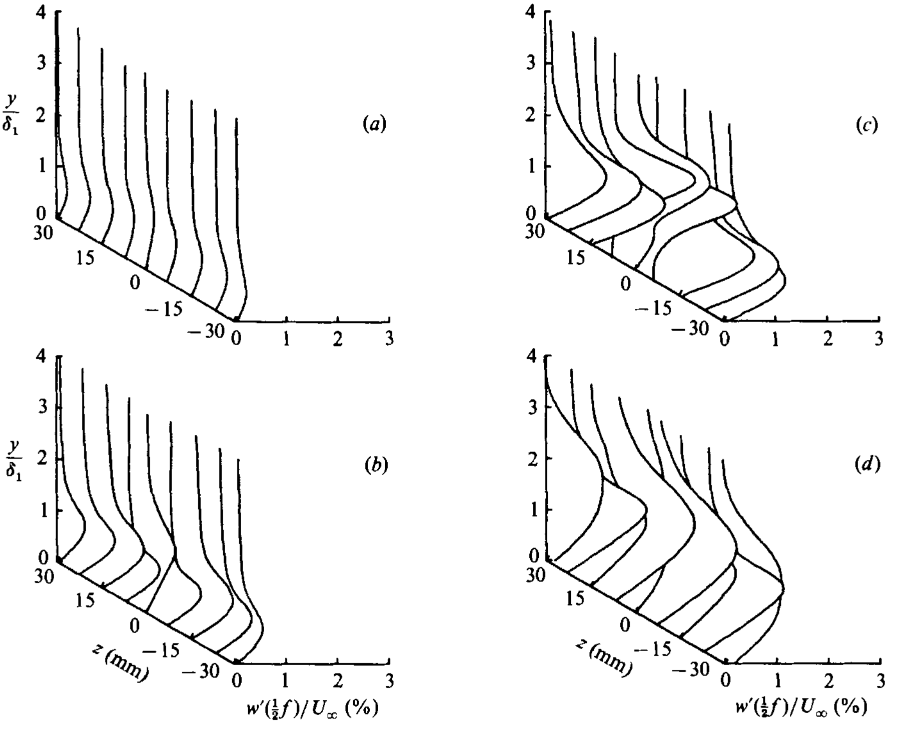

FIGURE 26. Spanwise distribution of subharmonic mode w-eigenfunction moduli at (a) $x = 115$, (b) 130, (c) 145 and (d) 160 cm for 150P condition.

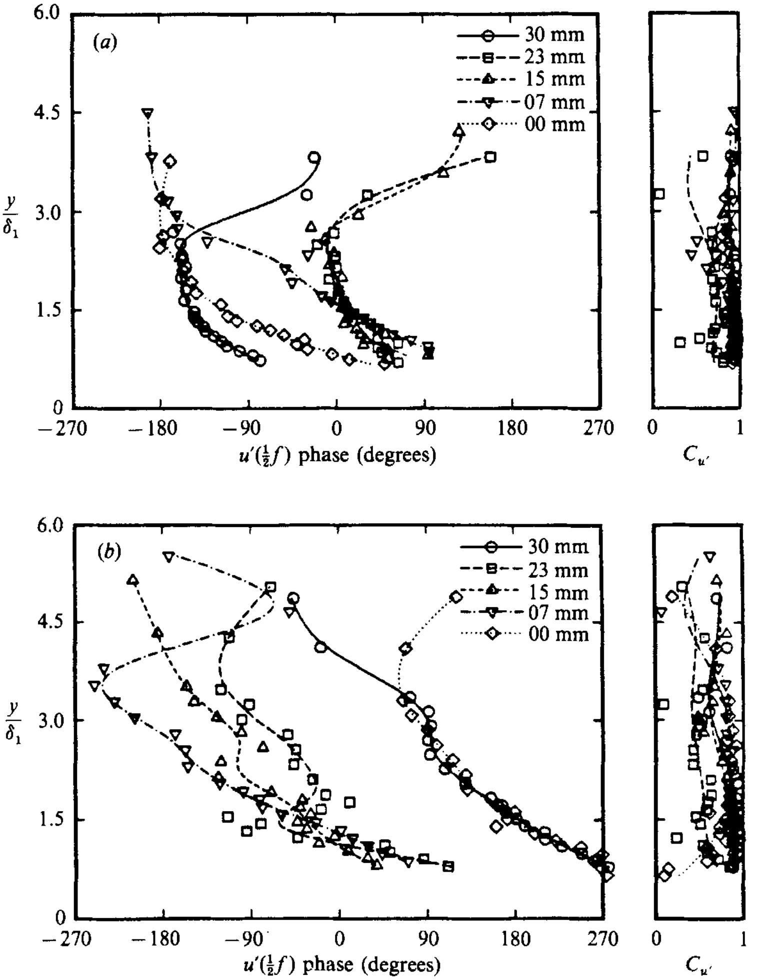

FIGURE 27. Spanwise distribution of subharmonic mode u-eigenfunction phase and linear coherence at (a) $x = 145$ and (b) 160 cm for 150P condition.

and v-fluctuations are a minimum. This can be clearly seen at the two positions (130 and 145 cm) upstream of energy saturation in figure 26. In addition, a peak away from the wall on the centreline is seen to develop. Directly on the centreline this is seen to decay as the flow passes the point of energy saturation.

In the process of development of the subharmonic mode, a number of nonlinear interactions are expected to take place. These result in the generation of other 3-D modes which are phase locked with the initial input modes. The dominant interactions documented in this investigation for input modes with wavenumbers $(\alpha, 0)$ and $(\frac{1}{2}\alpha, \pm\beta)$ were

$$(\alpha, 0) + (\tfrac{1}{2}\alpha, \pm\beta) = (\tfrac{3}{2}\alpha, \pm\beta), \quad (\tfrac{1}{2}\alpha, \pm\beta) + (\tfrac{1}{2}\alpha, \pm\beta) = (\alpha, \pm 2\beta),$$

$$(\tfrac{3}{2}\alpha, \pm\beta) + (\alpha, 0) = (\tfrac{5}{2}\alpha, \pm\beta), \quad (\tfrac{1}{2}\alpha, \pm\beta) - (\tfrac{1}{2}\alpha, \pm\beta) = (0, \pm 2\beta).$$

The streamwise phase development of the first three were presented in figure 16. The spanwise wavenumber of these three modes was verified from the spanwise

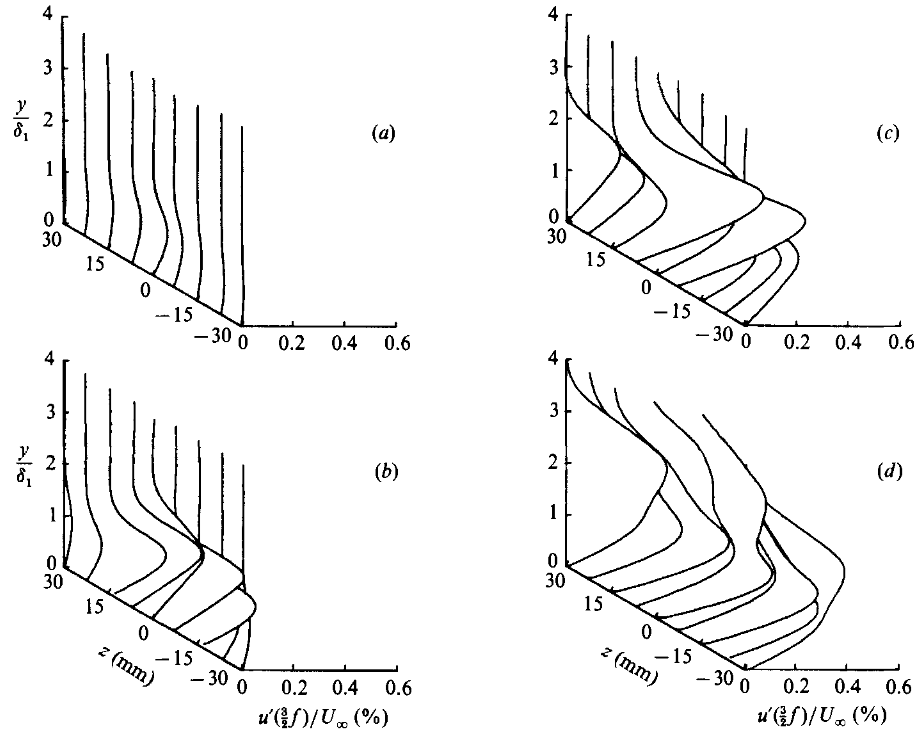

FIGURE 28. Spanwise distribution of $\frac{3}{2}f$ mode u-eigenfunction moduli at (*a*) $x = 115$, (*b*) 130, (*c*) 145 and (*d*) 160 cm for 150P condition.

distributions of the u-eigenfunction moduli shown in figures 28–30. These can be compared to the spanwise distribution of moduli of the subharmonic mode in figure 24. In that figure, the minima at the spanwise positions $z = \pm 23$ mm are indicative of the spanwise wavelength required to give a spanwise wavenumber $\beta\delta_1 = 0.205$.

For the $\frac{3}{2}f$ mode, the eigenfunction moduli show their three-dimensional character by the most upstream position, $x = 115$ cm, in figure 28. By $x = 145$ cm, clear minima are evident in span at $z = \pm 23$ mm, indicating the same spanwise wavenumber as the subharmonic. The spanwise distributions of the $\frac{5}{2}f$ eigenfunction moduli in figure 29 are somewhat slower to develop. However, by $x = 145$ cm, clear minima are evident at $z = \pm 23$ mm, indicating again the same spanwise wavenumber as the subharmonic mode.

On the cross-stream centreline of these two 3-D modes, their streamwise growth follows that of the subharmonic. At the point of subharmonic mode saturation ($x =$ 155 cm in figure 17), the maximum fluctuation level in these two modes was approximately 10 times smaller than the subharmonic with $u'_{3f/2} = 0.45$ and $u'_{5f/2} =$ 0.30. Kachanov & Levchenko (1984) had observed about the same factor difference between the subharmonic and $\frac{3}{2}$ modes, but in their case the $\frac{5}{2}$ mode was approximately 100 times smaller than the subharmonic level. They had not verified the spanwise wavenumber of these modes.

The spanwise distribution of the eigenfunction moduli for the mode at the TS frequency is shown in figure 30. At the most upstream position (upstream of Branch II) the spanwise distribution is almost uniform, except for a slight warping due to the growing subharmonic. By $x = 130$ cm, the spanwise variation has become more

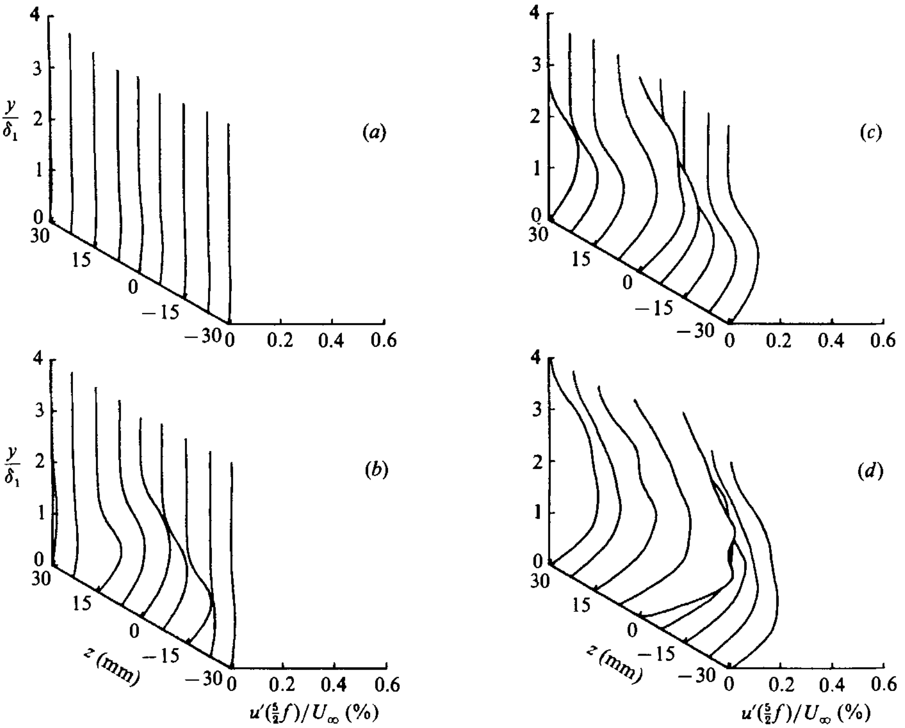

FIGURE 29. Spanwise distribution of $\frac{5}{2}f$ mode u-eigenfunction moduli at (a) $x = 115$, (b) 130, (c) 145 and (d) 160 cm for 150P condition.

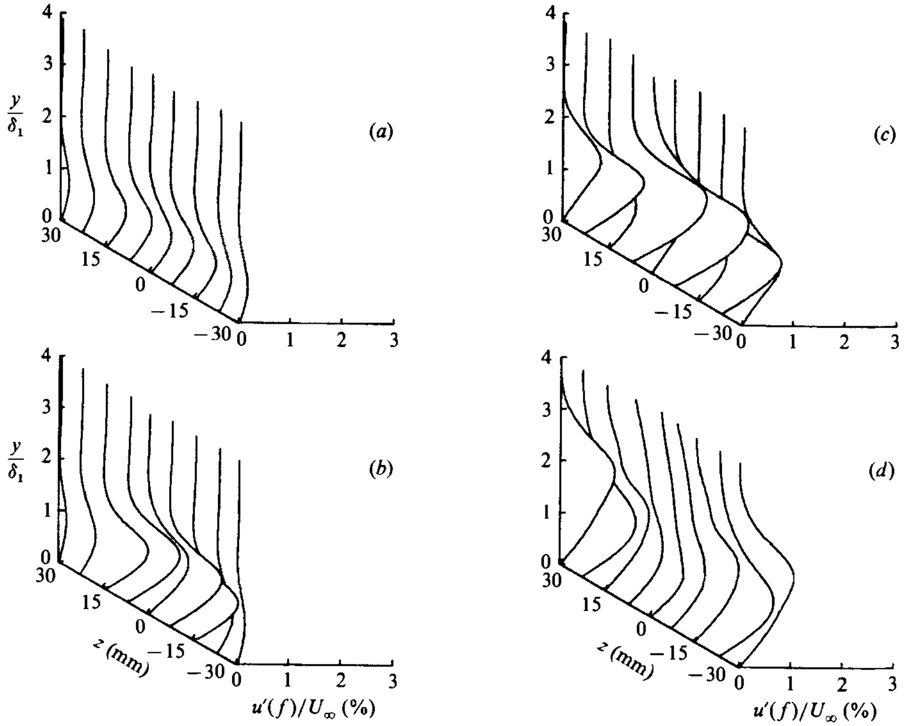

FIGURE 30. Spanwise distribution of fundamental mode u-eigenfunction moduli at (a) $x = 115$, (b) 130, (c) 145 and (d) 160 cm for 150P condition.

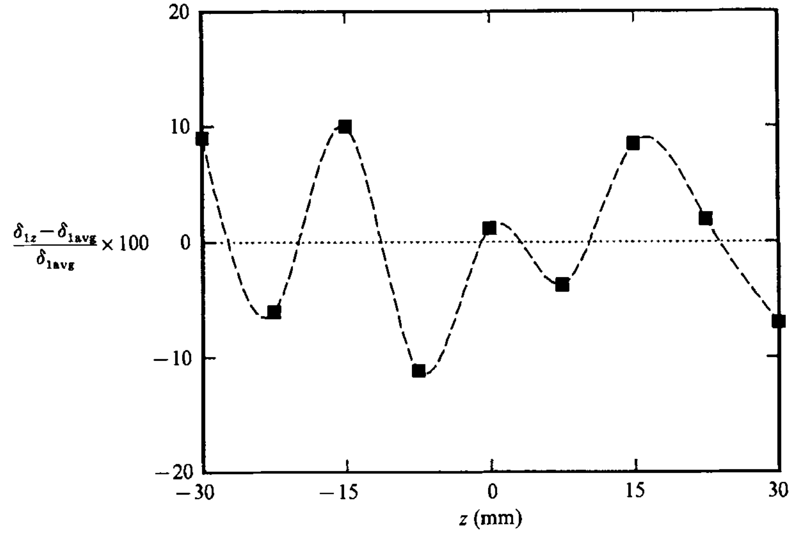

FIGURE 31. Percent spanwise variation of boundary-layer displacement thickness at $x = 145$ cm for 150P condition.

pronounced. By $x = 145$ cm three minima in span are visible. The distribution at $z = 0$ appears different because it coincides with the centre span of the subharmonic mode structure. The spanwise spacing of these three minima indicates a spanwise wavelength approximately one-half that of the subharmonic mode. In terms of the spanwise wavenumber, it is the harmonic value, $\pm 2\beta$, which was predicted in the summing interaction above.

One of the most interesting interactions is that which produces a spanwise variation of the mean flow, namely $(0, \pm 2\beta)$. A measure of this is the spanwise distribution of the time-averaged boundary-layer displacement thickness shown in figure 31. This is presented as the local percentage variation of the displacement thickness from the spanwise average at $x = 145$ cm.

Viewing the interacted modes as a whole, it is clear that their spatial character and x-development are similar to that of the subharmonic. Since the energy transfer is mediated by the subharmonic mode, the decrease in the fluctuation maximum at the centre span and movement away from the wall of the u-eigenfunction modulus at $x = 145$ cm should also be manifest in the interacted modes. This was indeed the case in all the interacted modes documented in these figures.

6.5. *Coherent motions*

The high degree of phase locking and spatial stationarity of the 3-D structures afforded by seeding initial 3-D disturbances allowed us to perform detailed phase reconstructions of the developing flow. In these, we have focused here on the most amplified 150P case. Figure 32 shows a time-series representation of phase-averaged uv-velocity vectors at two x-positions of 115 and 130 cm, which were well documented in previous figures. These are presented in the (y, x)-plane at the cross-stream intersection of oblique modes $(z = 0)$. In the Eulerian frame with time increasing from left to right in this figure, the flow direction is from right to left. The timescale covers three subharmonic cycles. The u- and v-scale is read from the isolated vector shown at the upper right side of each plot. Also, to better show details, the y-

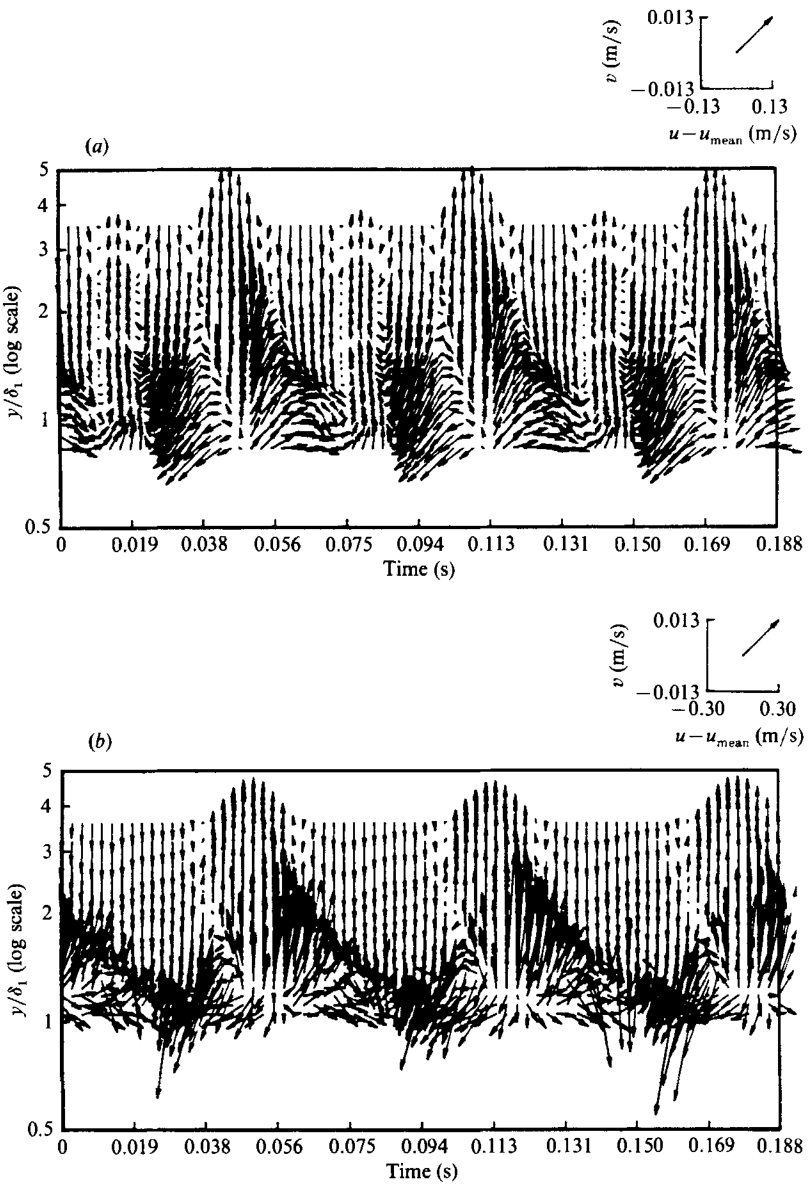

FIGURE 32. Phase-averaged reconstructions of uv-vectors time series at (a) $x = 115$ and (b) 130 cm, on $z = 0$ line for 150P condition.

coordinate has been expanded by a factor of ten compared to the x-scale of the subharmonic cycle, obtained by using the convection velocity.

At the upstream position, both fundamental and subharmonic modes are evident. The fundamental cycle corresponds to 12 time increments. On the outer part of the layer we observe a strong reinforcement of the positive v-component producing strong outward flow regions which are periodic with the subharmonic cycle. Near the wall, phase cancellations develop a stagnation line which forms at an angle to the flow direction. At the next x-position, figure 32(b), the stagnation line is very apparent as the dark intersection of upward- and downward-pointing vector arrow

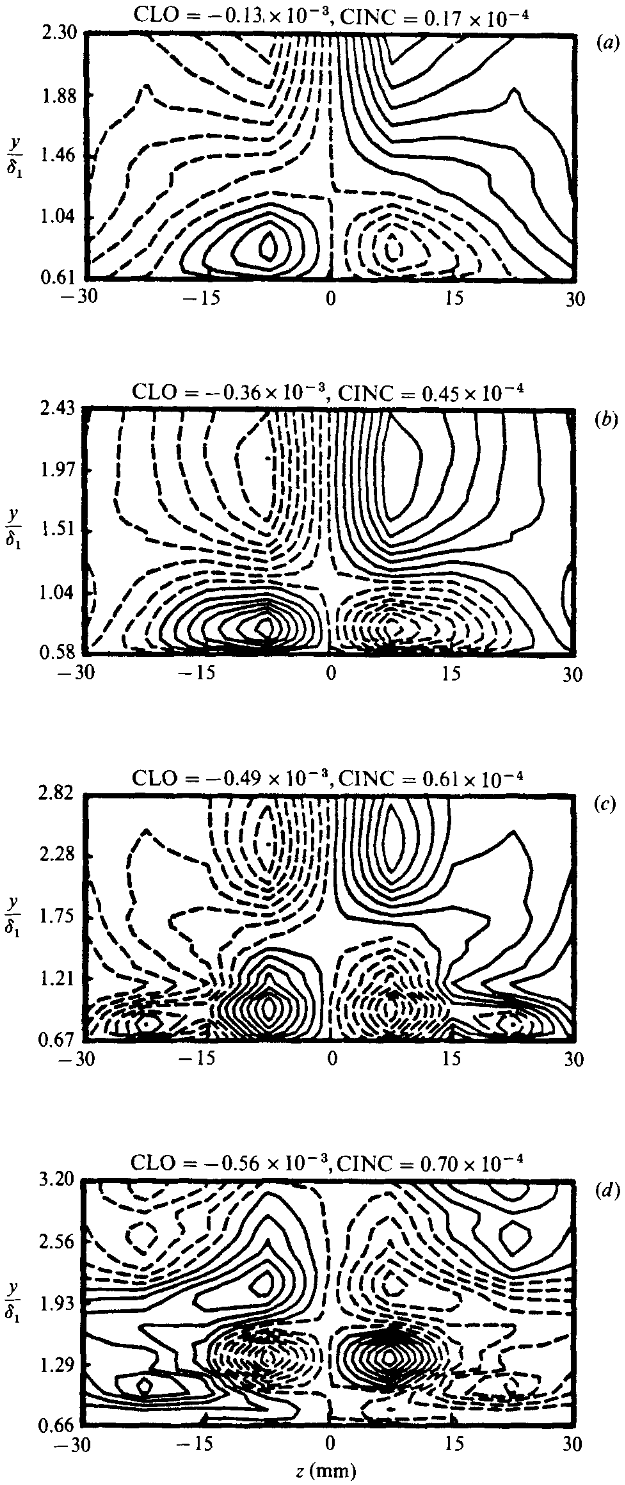

FIGURE 33. Phase-averaged reconstructions of vw-streamlines in (y, z)-plane at comparable representative time instants at (*a*) $x = 115$, (*b*) 130, (*c*) 145 and (*d*) 160 cm for 150P condition. (Data have been reflected about $z = 0$ line).

heads. The downstream side is raised away from the wall where fluid would encounter a higher mean velocity. The upstream side is displaced towards the wall into a lower mean velocity region. The resulting perturbation field is therefore the mechanism for the 3-D mode formation and stretching observed in the flow visualization records. In span, the locations of the peaks and valleys alternate with the 180° phase shifts of the subharmonic cycle. Past this x-position, this perturbation field remains relatively unchanged, even past energy saturation.

Although this view provides an accurate perspective of the development of the 3-D structure, it remains somewhat simplified because it does not account for the full three-dimensional nature of the flow. For example, at the locations of the oblique mode intersections, the contribution to the alternating v-component by the subharmonic is a maximum (figure 25). Off centre, the w-component becomes equally important (figure 26) and leads to a more complicated perturbation field. We attempt to bring out details of this through vw-streamlines in the (y,z)-plane. The full temporal development of these have been compiled by Mangano (1987). Only representative time (phase) instants are presented here, in figure 33, in order to give a sense of the coherent motions associated with the lambda structure. They correspond to time instants at the four x-positions for which eigenfunction moduli were presented in previous figures. They represent only one of the 24 encompassing a complete subharmonic cycle, but were selected to give a sense of the basic character of the organized motions and its increasing complexity as it progresses towards transition.

At the most upstream position ($x = 115$ cm), the streamlines depict cross-stream circulation patterns, with the outer circulation inducing that of the opposite sense near the wall. As a convention the dashed lined contours indicate circulation in the clockwise direction. The streamlines have units of m^2/s with the lowest level (CLO) and level increment (CINC) given at the top. The phase instant selected for this and the other three x-positions corresponds approximately to the point where the peak of the upstream structure overrides the valley of the downstream structure. In figure 32 at $x = 130$ cm, this corresponds to the time instant of 0.1 s. If one follows the pattern of streamlines in time, the direction of circulation in the outer part alternates in sign with the subharmonic cycle. The change in sign in the outer part disrupts the inner counter-circulation until it re-forms with the opposite sense in response to the outer flow.

By $x = 130$ cm, the strength of the cross-stream circulation has intensified, but the patterns are no more complex. With further x-development we observe an increased number of counter-rotating pairs with three at $x = 145$ cm and four at 160 cm. Recall that at the further x-position, the flow is past energy saturation and moving well towards a turbulent state. In the light of this, the degree of coherence of these motions is surprising. The full 3-D reconstructions of vortex lines and tracer particles performed by Corke & Dal-Ferro (1987) for some of these subharmonic resonance cases gives a more complete picture of the coherent motions associated with this later stage of transition.

6.6. *Nonlinear phase locking*

In order to further document the phase locking that existed between the subharmonic and 3-D modes produced by sum and difference interactions, cross-bicoherence estimates were calculated. Corke *et al.* (1989) had previously used this statistic to document the nonlinear interaction involved in vortex formation, pairing and feedback in an axisymmetric jet flow. Other investigators have made use of bispectral estimations to study other complex nonlinear flow systems such as transition to turbulence in a two-dimensional wake (Miksad *et al.* 1982; Miksad, Jones & Powers 1983; and Solis, Miksad & Powers 1986) and instability and feedback in an impinging shear layer (Knisely & Rockwell 1981). Because of the spatially changing energy levels in the modes of interest in this problem, the normalized bispectrum, or *bicoherence* was used. In this'.manner the emphasis was on the nonlinear phase locking which is necessary for efficient energy transfer between modes. To further emphasize the upstream influence and downstream development of spatially growing disturbances, the *cross-bicoherence* was calculated for spatially separated time series.

The cross-bicoherence (CBC) is defined as

$$\beta_{ijk}(\alpha_1, \alpha_2) = \frac{|\tilde{R}_{ijk}(\alpha_1, \alpha_2)|^2}{\langle|\tilde{u}_i(\alpha_1)|^2\,|\tilde{u}_j(\alpha_2)|^2\rangle\,\langle|\tilde{u}_k(\alpha_3)|^2\rangle},$$

where
$$\tilde{R}_{ijk}(\alpha_1, \alpha_2) = \langle\tilde{u}_i(\alpha_1)\,\tilde{u}_j(\alpha_2)\,\tilde{u}_k^*(\alpha_3)\rangle$$

is the cross-bispectrum, with i, j, and k equal to either i or j, referring to one of two mean removed time series, u, with wavenumbers α_1, α_2, and α_3 respectively. The notation $|\;|$ is the modulus of the component, $\sim$ denotes the transformed function in the wavenumber domain and $\langle\;\rangle$ the ensemble average. These wavenumbers are related to each other such that $\alpha_1+\alpha_2+\alpha_3 = 0$. In the present experiment, the time series were the streamwise velocity fluctuations, acquired at different spatial locations in the shear layer, $u(x, y, z, t)$, and at a fixed upstream reference. The reference used is the same ($x = 100$ cm) as for the linear phase and coherence estimates, such as in figure 16. For the case when i, j, and k are the same, that is a single time series, $\beta_{ijk}(\alpha_1, \alpha_2)$ will be symmetric with respect to α_1 and α_2, and will be referred to as the autobicoherence (ABC).

In the above equation, the calculation of the quantity

$$\langle|\tilde{u}_i(\alpha_1)|^2\,|\tilde{u}_j(\alpha_2)|^2\rangle$$

requires considerable computer time and memory storage. Therefore, it was convenient (and common) to replace it by

$$\langle|\tilde{u}_i(\alpha_1)|^2\rangle\,\langle|\tilde{u}_j(\alpha_2)|^2\rangle.$$

Justification for this substitution is given by Corke *et al.* (1989).

As with the linear coherence, the value of the CBC varies between 0 and 1. High values of the CBC indicate a high degree of triple phase locking

$$\theta_i(\alpha_1)+\theta_j(\alpha_2) = \theta_k(\alpha_3)$$

from realization to realization. Here $\theta_i(\alpha_1)$ is the instantaneous circular phase angle of $\tilde{u}_i(\alpha_1)$. The maximum level of the CBC estimate is however dependent on the signal-to-noise ratio of the data series. When no such phase locking exists the CBC has a value of zero.

The upper frequency limit of the cross-bicoherence is set by the Nyquist criterion, such that the sum of any two frequencies, f_1 and f_2, can not exceed half the sampling frequency. The region of validity takes the form of the bold outlined right-angled triangles (top and bottom) shown in figure 34. Other regions outside this, not exceeding the Nyquist limit, are omitted because of symmetry. The magnitude of the CBC is drawn as constant-level contours, in this case with values of 0.35, 0.65 and 0.85.

By our convention, in figures 34–39, the frequencies for the upstream reference,

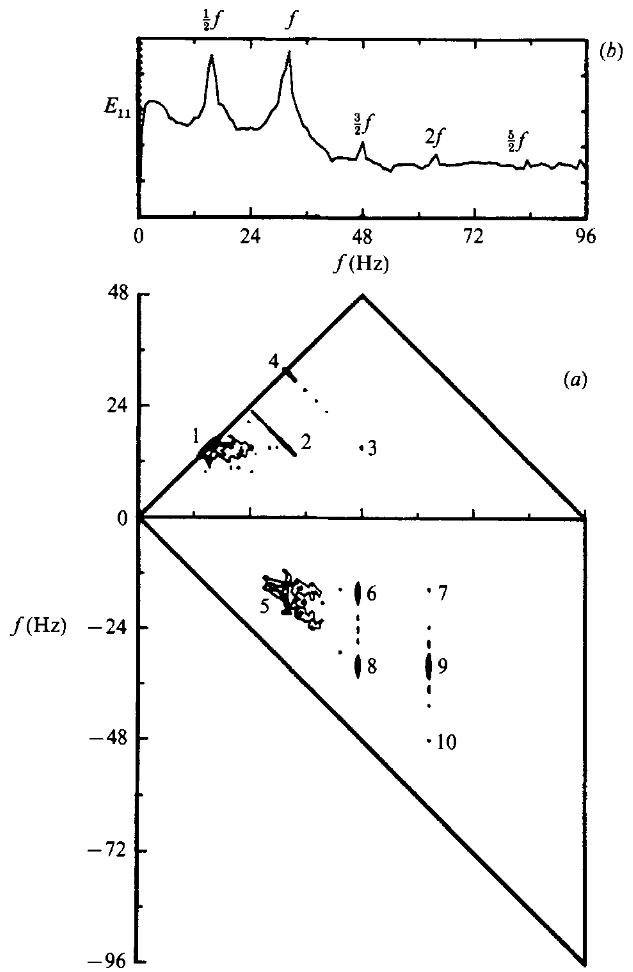

FIGURE 34. (a) Auto-bicoherence estimate and (b) autospectrum for streamwise velocity fluctuations at reference position, $x = 100$ cm, $z = 0$, y at position of maximum u', for 150P condition.

designated by subscript 1, are read from the abscissa. The frequencies read on the ordinate correspond to the downstream position and are designated by subscript 2. The ordinate frequencies are either added (top) to or subtracted (bottom) from those read on the abscissa to give the third frequency which is read as the intercept of a −45° line to the abscissa. The third frequency also corresponds to the downstream position (subscript 2). The downstream coordinate is indicated in the middle of the figure. For reference, above each of the CBC estimates appears the power spectra (in dB) of u-time series from the upstream fixed reference position and from the downstream position. These are shown as respective solid and dashed curves. They have been plotted so that the autospectra of the time series with changing x has been shifted downward 20 dB with respect to the reference autospectra. The full dynamic range of both is 50 dB. For the same resonance conditions, the reference spectra do not differ from one figure to the next. The dotted curve is the linear coherence between the upstream reference and downstream time series. Its ordinate value ranges from 0 to 1.

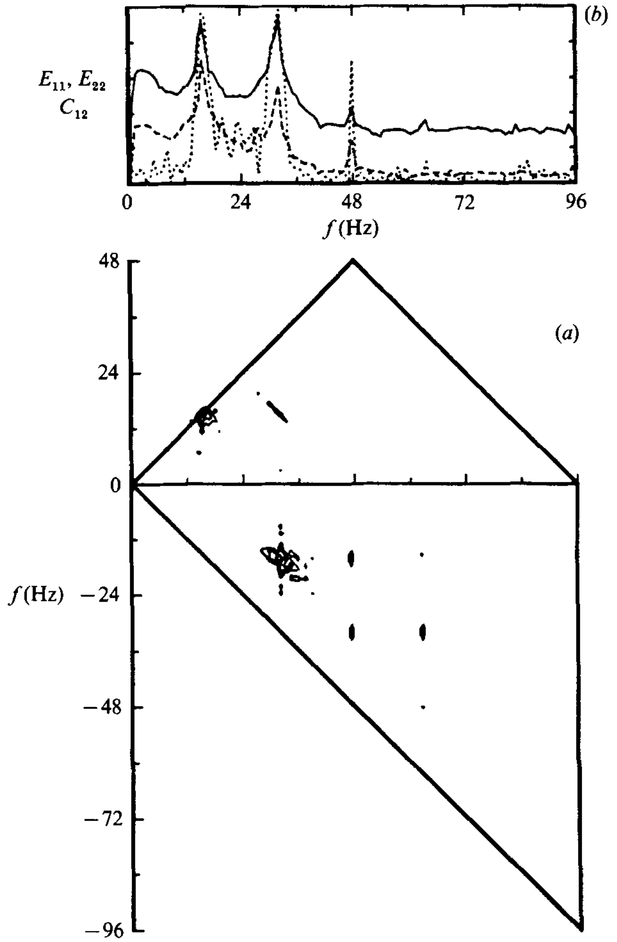

FIGURE 35. (*a*) Cross-bicoherence estimate and (*b*) autospectra and linear coherence at $x = 115$ cm, $z = 0$, y at position of maximum u'. Cross-statistics are with respect to reference position documented in figure 34.

Figure 34 documents the triple phase locking that existed in the sum and difference interactions listed in the previous section. These are shown in the form of the ABC for the time series at the reference position, $x = 100$ cm. The respective interactions have been numbered. In terms of the fundamental TS frequency, $f = 2\pi\alpha C_r$, these are

(1) $\frac{1}{2}f+\frac{1}{2}f = f$, (6) $\frac{3}{2}f-\frac{1}{2}f = f$,
(2) $f+\frac{1}{2}f = \frac{3}{2}f$, (7) $2f-\frac{1}{2}f = \frac{3}{2}f$,
(3) $\frac{3}{2}f+\frac{1}{2}f = 2f$, (8) $\frac{3}{2}f-f = \frac{1}{2}f$,
(4) $f+f = 2f$, (9) $2f-f = f$,
(5) $f-\frac{1}{2}f = \frac{1}{2}f$, (10) $2f-\frac{3}{2}f = \frac{1}{2}f$.

The lack of a peak for an interaction involving $\frac{5}{2}f$ suggests that phase locking with this mode was not significantly above the background levels.

Moving approximately three TS wavelengths downstream of the reference, the CBC in figure 35 document triple phase locking in space for all the above interactions

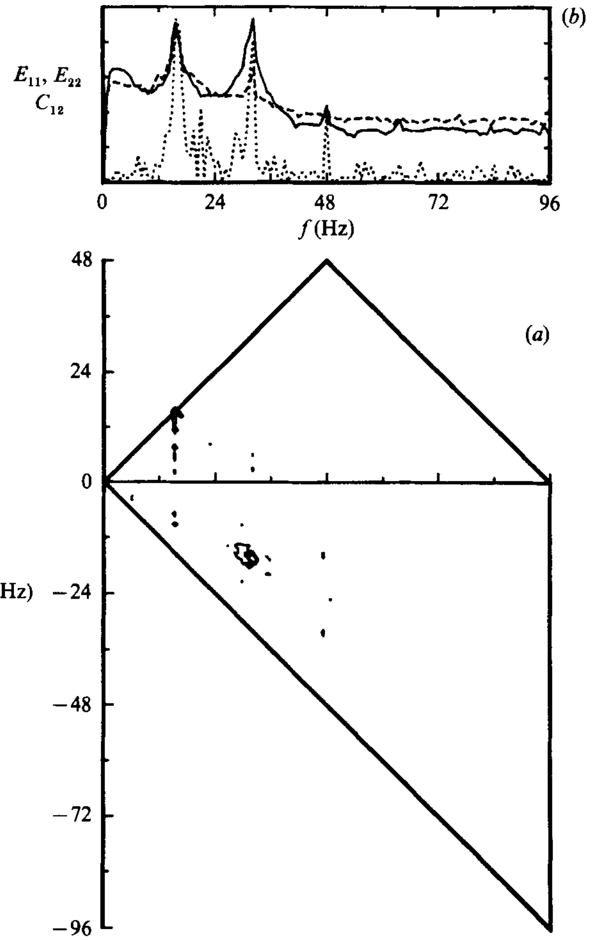

FIGURE 36. (a) Cross-bicoherence estimate and (b) autospectra and linear coherence at $x = 130$ cm, $z = 0$, y at position of maximum u'. Cross-statistics are with respect to reference position documented in figure 34.

except those corresponding to peaks 3 and 4. In the above interactions with the CBC, the first frequency refers to the reference position, the second and third refer to the downstream position. Therefore the lack of peaks 3 and 4 indicate a loss of significant phase locking with respect to the upstream reference in the second harmonic, $2f$, downstream. At the top of the figure, the autospectra (shifted down 20 dB) has about the same broad-band level as at the upstream position.

Another three TS wavelengths downstream, the autospectra at the top of figure 36 show an approximate 15 dB rise in the broad-band levels. The subharmonic mode has grown by approximately 10 dB. Beyond this x-position the subharmonic will continue to grow, but its rate of growth will decrease (figure 19). It is still however, four TS wavelengths upstream of the point of energy saturation (figure 17).

What can account for the rapid increase in broad-band fluctuations? To answer this we look to the bicoherence estimates. If all of the mode locking were confined to $\frac{1}{2}f$, f, $\frac{3}{2}f$, $2f$, the contours at these frequencies would be circular and of small diameter (to roughly the band width). In fact, the contours are substantially elongated. These document that the coherent modes are also nonlinearly phase locked with

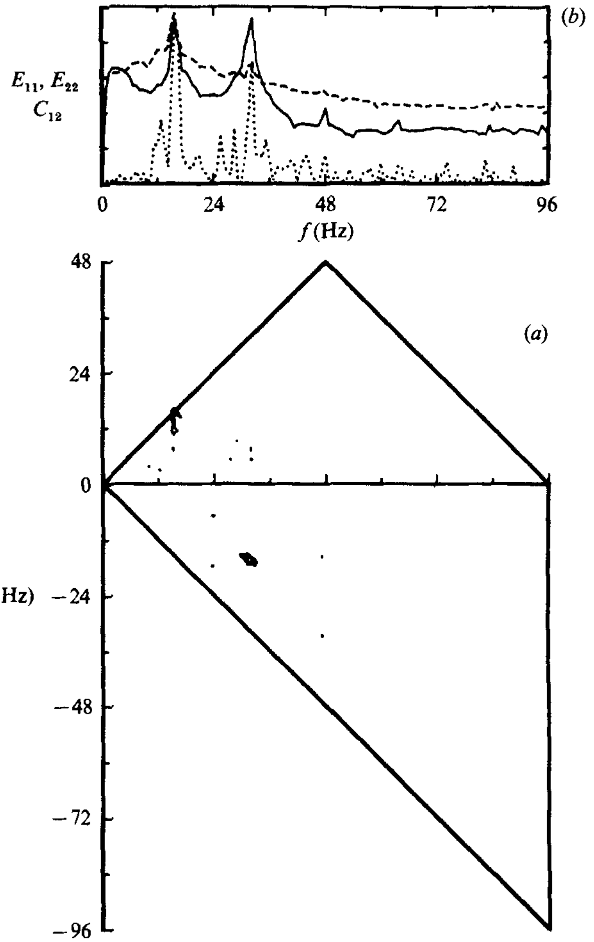

FIGURE 37. (*a*) Cross-bicoherence estimate and (*b*) autospectra and linear coherence at $x = 145$ cm, $z = 0$, y at position of maximum u'. Cross-statistics are with respect to reference position documented in figure 34.

harmonically centred broad-band modes. This effect is robust enough to remain significant over the span of distance of the three TS wavelengths corresponding to figures 34 and 35. In the case of the summed interactions, the −45° diagonal contours through peaks 2 and 3 in figure 36 involve frequencies in the band on either side of $\frac{1}{2}f$ and f which sum to produce the respective coherent modes $\frac{3}{2}f$ and $2f$. For the difference interactions, the nonlinear phase locking of these higher modes with the $\frac{1}{2}f$ side bands is seen as the vertically elongated contours. The combination of these shows how energy in an intermediate band of frequencies can be channelled to both higher and lower frequencies. This basic process is mediated by the primary fundamental/subharmonic interaction.

With increasing downstream distance and increased subharmonic amplitude, the range of broad-band modes is seen to shift towards lower frequencies. This is seen clearly in figure 36 as the vertical band at upstream subharmonic frequency. The significance of the vertical orientation is that this lower-frequency band of modes is not in the upstream reference, read on the abscissa. Where did they originate? the CBC estimate at the x-position immediately upstream (figure 35) indicates that they

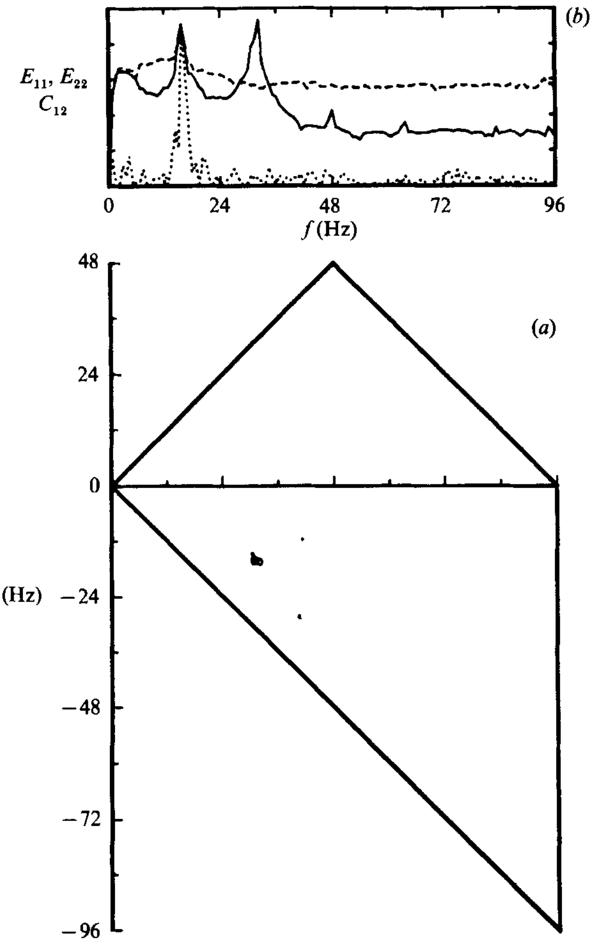

FIGURE 38. (*a*) Cross-bicoherence estimate and (*b*) autospectra and linear coherence at $x = 160$ cm, $z = 0$, y at position of maximum u'. Cross-statistics are with respect to reference position documented in figure 34.

came about through difference interactions with the higher-frequency subharmonic side bands of peak 5. At the downstream position, these lower frequencies interact with the subharmonic to fill the band of frequencies between $\frac{1}{2}f$ and f (summed) and below $\frac{1}{2}f$ (differenced). The effect of this is seen in the autospectra at the next downstream station in figure 36 as the further growth of energy in these bands.

Recall that the x-position in figure 37 is still two TS wavelengths upstream of energy saturation. The higher broad-band levels now present have diminished the phase locking with the upstream reference except in narrow bands around f and $\frac{1}{2}f$ modes. The band below peak 1 leads to the loss of phase coherence with the fundamental that is observed at the next x-position, past energy saturation, in figure 38. Except for the phase locking that still exists for the subharmonic, the spectrum is quite broad band and sharply contrasted to the upstream reference spectrum.

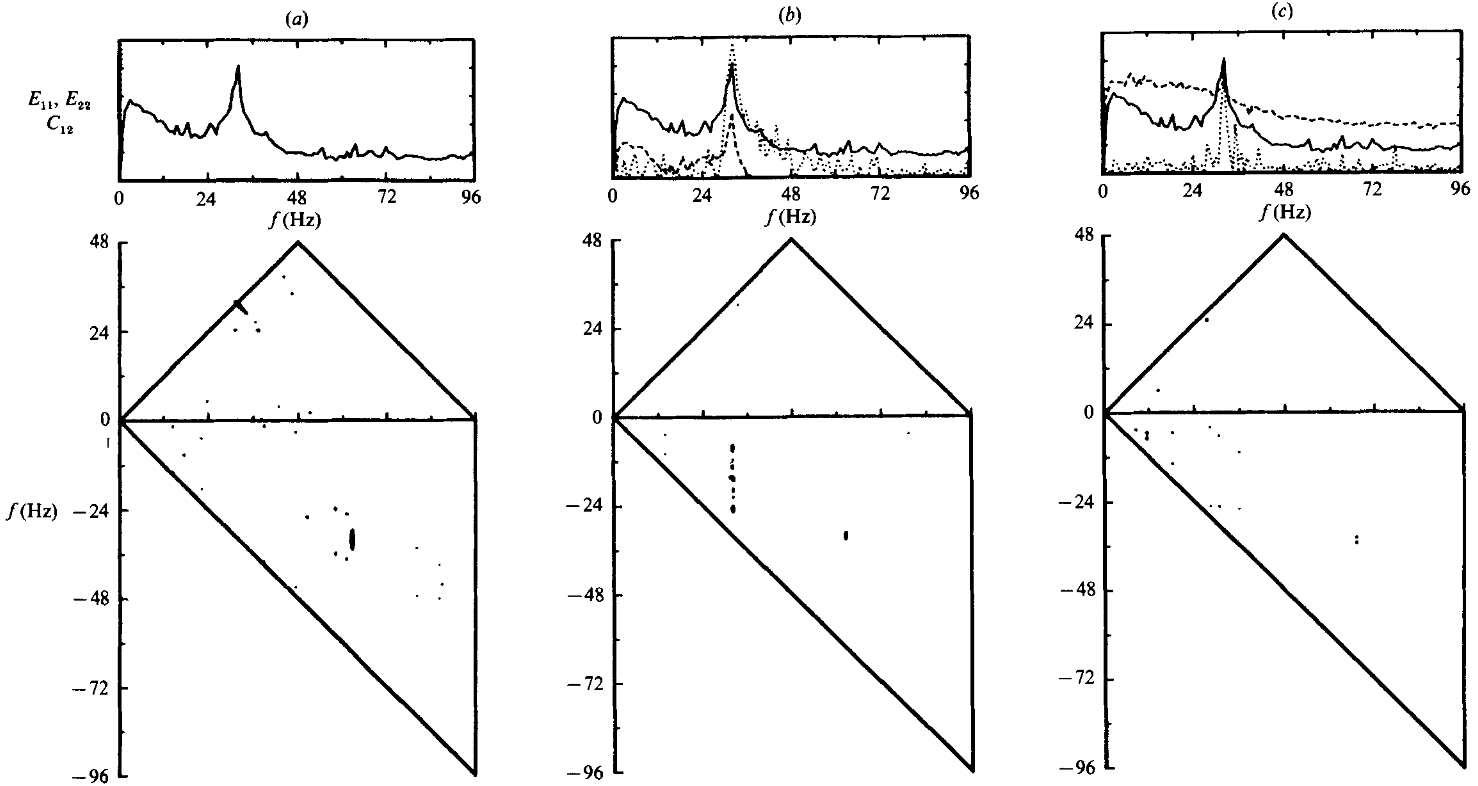

FIGURE 39. Bicoherence estimates, autospectra and linear coherence at representative x-positions along $z = 0$ line, at y-position of maximum u', in 2-D only seeded condition. x-Positions are the reference (a) $x = 100$ cm, (b) $x = 130$ cm and (c) $x = 160$ cm.

6.7. *Natural subharmonic mode development*

To this point we have purposely looked at the subharmonic resonance mechanism and transition to turbulence with specific 3-D input wavenumber content in order to fully define the state of the flow and to fully phase lock the growing modes everywhere in space. In natural transition with stochastic inputs, we can hardly expect the flow to be so well behaved. We therefore want to contrast the results in boundary layers with 3-D mode seeding to produce subharmonic resonance, to those with a natural subharmonic interaction. To do this we consider a case where only 2-D TS modes are seeded. We chose this case over a fully natural (unforced) case, because the plane TS cycle provides a phasing signal which could be used for spatial cross-statistics. This type of forcing is of course similar to the more traditional approach such as by Kachanov & Levchenko (1984) and Saric & Thomas (1983).

The TS-only forced case we chose has the same TS frequency and initial amplitude as the 150P case so that they offer a direct comparison. This case has been previously documented in figures 10–13. The bicoherence estimates are presented at three x-positions in figure 39. At the reference position ($x = 100$ cm in figure 39*a*), the ABC documents a triple phase locking of the fundamental with its harmonic only. This can be contrasted to the ABC in figure 34. Six TS wavelengths downstream this interaction diminishes and the CBC in figure 39(*b*) document a broad band of modes which are nonlinearly phase locked with the TS mode. At the centre of this band is the TS subharmonic mode. The resonance interaction with the subharmonic and broad side bands in this case lead to a very rapid spectral filling (figure 39*c*). In this case the subharmonic mode does not reach a high saturation level, less than 1 %, which is comparable with what has been seen by others for natural subharmonic mode transition. It appears that the side-band interactions with the fundamental have in this case spread energy rapidly and efficiently to reduce the large-amplitude growth of the subharmonic.

7. Discussion

7.1. *Growth of 3-D disturbances*

As pointed out in §1, one of the primary motivations of this experiment was to study fundamental processes leading to the first growth of three-dimensional modes leading to the transition to turbulence. Here we focused on subharmonic resonance mechanisms attributed to both Craik (1971) and Herbert (1983*b*).

Previous experiments studying the growth of 3-D modes in boundary layers have used vibrating ribbons or wires which were designed to primarily excite 2-D TS modes of prescribed frequency and streamwise wavenumber. The ultimate development of 3-D states occurred through uncontrolled processes. For a fixed TS frequency, the only other parameter that these experiments could vary was the initial amplitude. A general approach, it seems, was to increase the initial amplitude so that 3-D modes and breakdown could be achieved before the end of the test section. In the cases of Klebanoff & Tidstrom (1959), Klebanoff *et al.* (1962) and Williams, Fasel & Hama (1984) a relatively large initial amplitude, u'/U_∞, of approximately 1 % was used.

Primed by the results of Saric & Thomas (1983), we took special care to keep a low initial forcing amplitude of both the 2-D and 3-D modes in our present experiment. As described in §4, the levels were adjusted to achieve transition to turbulence in the most amplified case (150P) and kept fixed for all other cases, even if transition was not fully achieved. For the first time in a study like this, we could adjust both the 2-D and 3-D amplitudes separately. Our approach was to set an initial amplitude for the 3-D subharmonic mode and adjust the 2-D initial amplitude to achieve saturation of the subharmonic within the last third of the test section length. With some experience, we found that if we 'over-forced' the 3-D subharmonic mode, we observed a subharmonic mode downstream with a harmonic spanwise wavenumber ($\frac{1}{2}\alpha$, $\pm 2\beta$). An interesting characteristic was that under these conditions the flow was able to sustain a much larger fluctuation level before energy saturation. Although the regular subharmonic ($\frac{1}{2}\alpha$, $\pm\beta$) development looked well behaved, the emergence of this other mode was not explainable through simple nonlinear interactions of the principle input modes $(\alpha, 0)$ and ($\frac{1}{2}\alpha$, $\pm\beta$). One possible interaction to produce this was between the primary subharmonic and a mode with wavenumbers (α, $\pm\beta$). The origin of this mode might come about from the generation of a higher harmonic with the larger initial 3-D subharmonic input. To avoid this, we purposely kept the level of the 3-D mode seeding below a value needed to produce the ($\frac{1}{2}\alpha$, $\pm 2\beta$) mode downstream. In future experiments we plan to investigate this in more detail.

Table 1 documents the initial temperature perturbation level for the 3-D modes in all cases to be 0.31 %. Using the analogy of the equivalence between the unsteady heating and v-fluctuation intensity, the initial velocity perturbation produced by unsteady heating of this magnitude was estimated to be approximately 0.07 %. This was only just above what we consider to be the base disturbance level of the wind tunnel. Such a very low level is only required because we provided a perfect coherent phase locking between the 2-D and 3-D modes which promoted the strongly nonlinear resonance mechanism.

At Branch II of the neutral stability curve, the u'/U_∞ level of the fundamental mode is only approximately 0.25 %, as taken from figure 17 for the 90P case where resonance has not yet occurred by Branch II. At this same x-location, the 3-D subharmonic was highly damped and was at an amplitude level of less than 0.05 %. These amplitudes are well below the 0.3 % limit observed by Saric & Thomas to produce C-type modes, and are considerably below levels previously used by others investigating 3-D mode breakdown and transition to turbulence.

What is the significance of the amplitude thresholds for the selection between C-, H- and K-type modes? In our cases, for the same initial amplitudes of TS and oblique modes, the characteristics of the 3-D modes was dictated by the wavenumber content (streamwise and spanwise) of the seeded inputs. The dependence on the ratio of streamwise to spanwise wavenumber was shown in figure 19(*b*).

If the energy in free-stream disturbances in our tunnel were evenly distributed over a wide range of 3-D wavenumbers, then we should expect that the 3-D features that would emerge through an interaction with TS modes would have a spanwise wavenumber approximately that of the 150P case. That is, for the same initial amplitude level, this is the more amplified 3-D state. The fact that we could observe the emergence and document the less amplified, smaller spanwise wavenumber 90P condition was because we put greater energy into those spanwise wavelengths, and thereby exceeded the background levels of other more amplified 3-D modes.

In the present experiment, when seeding specific streamwise *and* spanwise wavenumbers, the effect of initial amplitude would only advance the point of subharmonic energy saturation and ultimate breakdown upstream. Under such controlled conditions, this is the expected behaviour. Under less controlled conditions, the effect of initial amplitude, or to a greater extent of an exact initial amplitude threshold, on the natural selection of spanwise wavelengths of 3-D subharmonic modes clearly must also depend on the character of the free-stream disturbances.

In all cases, at our levels of initial forcing, we never observed fundamental (K-type) transition. K-type appears to result only with much larger levels of initial TS-mode forcing and/or in the presence of coherent steady longitudinal vorticity as in the case of the numerical simulations of Singer, Ferziger & Reed (1986). Since neither of these were present in this experiment, the absence of K-type behaviour is expected.

One of the goals of this investigation was to try to delineate between the two basic theoretical mechanisms, C- and H-type. The conditions for that comparison primarily correspond to the 90P and 150P cases. Table 2 documents some of their experimentally derived characteristics. One of the basic requirements for C-type is that the interacting subharmonic 3-D mode must have the same phase velocity as that of the fundamental TS mode. For a 3-D Orr–Sommerfeld mode, the phase speed depends on the spanwise wavenumber and Reynolds number. In our experiment, the 90P and 150P cases were conducted at the same Reynolds numbers, with the same streamwise wavenumbers. The wave numbers in table 2 were made dimensionless using the displacement thickness at $Re_{\delta_1} = 1250$. Comparisons to linear temporal theory are made at $Re_{\delta_1} = 1000$ where $\delta_1 = 2.4$ mm. At this Reynolds number, the 180P case has $\alpha_1 \delta_1 = 0.24$, $\alpha_{\frac{1}{2}} \delta_1 = 0.12$ and $\beta_{\frac{1}{2}} \delta_1 = 0.22$. Linear theory predicts phase speeds $(C_r/U_\infty)_1 = 0.35$ and $(C_r/U_\infty)_{\frac{1}{2}} = 0.39$. Similarly, for the 90P case, $\alpha_1 \delta_1 = 0.20$, $\alpha_{\frac{1}{2}} \delta_1 = 0.10$ and $\beta_{\frac{1}{2}} \delta_1 = 0.125$ yielding $(C_r/U_\infty)_1 = (C_r/U_\infty)_{\frac{1}{2}} = 0.34$; and 150P case, $\alpha_1 \delta_1 = 0.20$, $\alpha_{\frac{1}{2}} \delta_1 = 0.10$ and $\beta_{\frac{1}{2}} \delta_1 = 0.164$ yielding $(C_r/U_\infty)_1 = 0.34$ and $(C_r/U_\infty)_{\frac{1}{2}} = 0.36$. For the 90P case, we have used the spanwise wavenumber for the expected 45° wave angle, since, when the full eigenfunction profiles were examined in the 150P and 180P cases (C designation), the expected wave angles (bracketed) were obtained.

The measured phase velocity for the TS mode in the 180P case is within 3% of the expected value. For the 90P and 150P the agreement is not as good (approximately an 11% difference). The difficulty arises in our experiment due to finite-spaced measurement stations which limited the number of streamwise samples of phase. For the 180P case, we were able to take more finely spaced streamwise increments for the phase measurements (Mangano 1987) which undoubtedly lead to a better agreement with theory.

Of the three cases examined, only the 90P satisfies the Craik resonance criterion, namely, equal phase velocities between the fundamental plane TS and subharmonic oblique modes. In that case, we indeed documented the resonant growth of the subharmonic mode.

For our other two cases (150P and 180P), subharmonic resonance was also documented. These two clearly do not satisfy Craik's criterion, that is, by our selection of spanwise wavenumber, the wave-propagation properties with respect to the fundamental TS mode are suitably different. Examination of the streamwise phase development for fundamental and subharmonic modes in these two cases (150P in figure 16) verified that the subharmonic mode (as well as other interacted modes) had reached a phase-velocity synchronization with the fundamental TS, independent of their spanwise wavelengths. This observation is in complete agreement with Herbert and not explainable by Craik's mechanism. Calculations for the conditions of these two cases have recently been performed by Crouch (1988, Figs. 4.23 and 4.24). These show good agreement between experiment and theory in regard to the streamwise growth of the fundamental TS and 3-D subharmonic modes. In the case of the most amplified condition, the correspondence is especially good even up to the point of subharmonic energy saturation. The dependence of the maximum subharmonic amplification on the ratio of streamwise to spanwise wavenumber (seen in figure 19*b*) was also accurately predicted (dotted) for H-type conditions by Bertolotti & Herbert (1985).

7.2. *Nonlinear interactions and transition to turbulence*

With the downstream growth of the subharmonic 3-D mode, we have documented basic changes in its character which we associate with its nonlinear development and transition to turbulence. These have included a movement of the subharmonic eigenfunction modulus maximum away from the wall to a point above the height of the critical layer, and an altering of the eigenfunction phase distribution from 'wave-like' to 'structure-like'. Coincident with this was a similar change in the eigenfunction character of the initial fundamental wave prompting the growth of a new 3-D mode at the initial fundamental frequency, with harmonic spanwise wavenumber, $\pm 2\beta$. Other interacted modes included $(\frac{3}{2}\alpha, \pm\beta)$, $(\frac{5}{2}\alpha, \pm\beta)$ and $(0, \pm 2\beta)$.

The subharmonic mode grows to a high level but eventually saturates, and beyond that point decays. In this process, the modes nonlinearly phase locked with the subharmonic shift toward lower frequencies. These lower-frequency modes were traced to broad side bands on the initial fundamental and subharmonic modes and higher-harmonic coherent sum and difference modes. The origin of these is presumably small imperfections in mode tuning produced by stochastic input from free-stream disturbances. This picture of the source of low-frequency components is consistent with the explanation given by Kachanov & Levchenko (1984). At the end of this stage the velocity spectrum is quite broad band, and the mean profile is more full indicating an increase in the viscous drag and a decrease in the shape factor. These characteristic changes first appear on the centreline of subharmonic lambda structures, and eventually progress outward in span from individual structures.

In the process of subharmonic mode growth, the two fundamental points of development were the location of maximum subharmonic amplification, and subharmonic energy saturation. The former marked the approximate location of the first appearance of 3-D modes in the flow visualization records. The location of these depended on the initial amplitudes of the seeded modes and on their streamwise and spanwise wavenumbers. In the 180P case, these two points closely coincided. This was found to result in extra strong nonlinear phase locking with higher-frequency discreet modes.

Similarly low-frequency sum and difference interactions and subharmonic side-band frequencies were documented with less well controlled conditions of only 2-D TS forcing. In this case these contributed to lower-frequency difference interactions and broad-band spectral filling at a more rapid rate than with the controlled 3-D cases. This apparently accounts for the limited maximum fluctuation level that the flow can sustain prior to the growth of broad-band modes in natural subharmonic transition seen here and by others. The maximum level of total velocity fluctuations in our case was only approximately one third that of the 3-D seeded cases.

For subharmonic mode transition to turbulence, the method of 'breakdown' was found to be fundamentally different from that attributed to K-type. Most notably the change of phase velocity which occurred upstream of energy saturation, the high inflexional mean profile, the form of the y-eigenfunction phase distribution, and the generation of large-amplitude regular high frequencies past energy saturation, observed for K-type transition were not present here. For subharmonic transition, irregular higher-frequency components are observable in the time traces when the subharmonic energy is sufficiently large and nonlinear behaviour is evident. This can occur well upstream of subharmonic saturation and upstream of where the mean profile first deviates from a Blasius one. Some of these frequencies are attributable to sum and difference interactions with the subharmonic mode, as described earlier. The broad-band frequencies begin to fill the layer starting from the wall and first appear at the cross-stream centre of lambda structures. By the point of subharmonic energy saturation, time traces on the centreline show broad-band frequencies at all parts of the subharmonic cycle, not just on the high-velocity part as for the fundamental with K-type.

The basic difference between these two forms of transition is that for subharmonic breakdown, the resonant interaction between two modes allows an efficient mechanism for intercomponent energy transfer and early spectral broadening not present for fundamental mode (K-type) breakdown. By this approach the breakdown process can be explained through a secondary instability of basic modes rather than through higher-order (tertiary or quartic) instabilities mechanisms often attributed to higher-frequency mode generation in K-type. In the scenario presented here, the flow does not 'violently break down' but rather progresses through a natural sequence of sum and difference interactions leading to a smooth merging to a turbulent state.

8. Conclusions

Subharmonic resonance was the mechanism for the growth of 3-D modes in a Blasius boundary layer. This involved an interaction between initial TS waves at a fundamental frequency, and pairs of subharmonic oblique waves of equal angles and opposite sign. These modes were produced by a spanwise array of heating wires placed near the critical layer. Through software control, the spanwise wavenumbers of oblique modes was variable. The interaction was marked by a matching of phase velocities, resonant energy exchange and enhanced growth of the subharmonic mode leading eventually to large amplitudes and energy saturation. For different spanwise wavenumbers, the maximum amplification rate was in good agreement with predictions arising from an H-type mechanism.

With the growth of the subharmonic mode, other nonlinear 3-D interacted modes were produced. Their streamwise and spanwise wavenumbers had been experimentally verified. Owing to the spatial stationarity afforded by the 3-D mode seeding, phase averaging brought out the coherent motions associated with the staggered lambda structures observed in flow visualization. The eventual saturation of the subharmonic mode was marked by a loss of precise phase locking between the subharmonic mode and higher interacted modes. This initially stemmed from fundamental-mode side bands which acted through sum and difference interactions with the subharmonic to produce low-frequency broad-band modes. Downstream, these modes interacted with the subharmonic to gradually fill the spectrum. With low initial amplitudes, this is expected to be the chief scenario for the natural growth of three-dimensionality and transition to turbulence in most boundary-layer flows.

The authors wish to express thanks to colleagues who have especially influenced this work by their past discussions and frequent input, especially Mark Morkovin and Hassan Nagib. The work of Bill Saric first led us to look at this problem. The numerous discussions with Thorwald Herbert have helped us to keep our direction.

This work is supported by a grant from the Air Force Office of Scientific Research, F49620-86-C-0133, which is monitored by Dr James McMichael.

REFERENCES

BAR-SEVER, A. 1984 Boundary layer transition over rough surfaces. M.S. thesis, Illinois Institute of Technology.

BENNEY, D. J. 1964 Finite amplitude effects in an unstable laminar boundary layer. *Phys. Fluids* **7**, 319.

BENNEY, D. J. & LIN, C. C. 1960 On the secondary motion induced by oscillations in a shear flow. *Phys. Fluids* **3**, 656.

BERTOLOTTI, F. 1985 Temporal and spatial growth of subharmonic disturbances in Falkner–Skan flows. M.S. thesis, Virginia Polytechnic Institute State University.

CORKE, T., BAR-SEVER, A. & MORKOVIN, M. 1986 Experiments on transition enhancement by distributed roughness. *Phys. Fluids* **29**, 3199.

CORKE, T. & DAL-FERRO, P. 1987 Later stages of transition in three-dimensional seeded boundary layers. *IIT Fluid Dynamics Center Rep.* 87–2. (In preparation for *J. Fluid Mech.*)

CORKE, T., KOGA, D., DRUBKA, R. & NAGIB, H. 1977 A new technique for introducing controlled sheets of smoke streaklines in wind tunnels. *IEEE Publication* 77-CH 1251-8 AES.

CORKE, T. & MANGANO, R. 1987 Transition of a boundary layer: controlled fundamental–subharmonic interactions. In *Turbulent Management and Relaminarization, IUTAM Symp. Bangalore, India*, pp. 199–213. Springer.

CORKE, T. C., SHAKIB, F. & NAGIB, H. M. 1985 Effects of low amplitude forcing on axisymmetric jet flows. *AIAA Shear Flow Control Conf., Boulder, Colorado, AIAA*-85-0573.

CORKE, T. C., SHAKIB, F. & NAGIB, H. M. 1989 Mode selection and resonant phase locking in unstable axisymmetric jets. *J. Fluid Mech.* (submitted).

CRAIK, A. D. D. 1971 Nonlinear resonant instability in boundary layers. *J. Fluid Mech.* **50**, 393.

CROUCH, J. D. 1988 The nonlinear evolution of secondary instabilities in boundary layers. Ph.D. thesis, Virginia Polytechnic Institute State University.

DAL-FERRO, P. 1987 Later stages of transition in three dimensional seeded boundary layers. M.S. thesis, Illinois Institute of Technology.

HAMA, F. R. 1960 Boundary-layer transition induced by a vibrating ribbon on a flat plate. In *Proc. 1960 Heat Transfer and Fluid Mechanics Institute*, p. 92. Stanford University Press.

HASSELMAN, K., MUNK, W. & MCDONALD 1963 Bispectrum of ocean waves. In *Proc. Symp. on Time Series Analysis* (ed. M. Rosenblatt), pp. 125–139. Wiley.

HERBERT, TH. 1983*a* Secondary instability of plane channel flow. *Phys. Fluids* **26**, 871.

HERBERT, TH. 1983*b* Subharmonic three-dimensional disturbances in unstable plane shear flows. *AIAA paper* 83-1759.

HERBERT, TH. 1988 Secondary instability of boundary layers. *Ann. Rev. Fluid Mech.* **20**, 487.

HERBERT, TH. & BERTOLOTTI, F. 1985 The effect of pressure gradients on the growth of subharmonic disturbances in boundary layers. In *Proc. Conf. Low Reynolds Number Airfoil Aerodyn.* (ed. T. Mueller), pp. 65–76. Notre Dame University.

HERBERT, TH. & MORKOVIN, M. V. 1980 Dialogue on bridging some gaps in stability and transition research. In *Laminar–Turbulent Transition* (ed. R. Eppler and H. Fasel), p. 47. Springer.

HINICH, M. J. & CLAY, C. S. 1968 The application of the discrete Fourier transform in the estimation of power spectra, coherence, and bispectra of geophysical data. *Rev. Geophys.* **6**, 347.

KACHANOV, YU. S., KOSLOV, V. V. & LEVCHENKO, V. YA. 1977 Nonlinear development of a wave in a boundary layer. *Fluid Dyn.* **12**, 383.

KACHANOV, YU. S. & LEVCHENKO, V. YA. 1984 The resonant interaction of disturbances at laminar–turbulent transition in a boundary layer. *J. Fluid Mech.* **138**, 209.

KELLY, R. E. 1968 On the resonant interaction of neutral disturbances in inviscid shear flows. *J. Fluid Mech.* **31**, 789.

KLEBANOFF, P. S. & TIDSTROM, K. D. 1959 Evolution of amplified waves leading to transition in a boundary layer with zero pressure gradient. *NASA Tech. Note* D195.

KLEBANOFF, P. S., TIDSTROM, K. D. & SARGENT, L. M. 1962 The three-dimensional nature of boundary-layer instability. *J. Fluid Mech.* **12**, 1.

KNISELY, C. & ROCKWELL, D. 1981 Self-sustained low-frequency components in an impinging shear layer. *J. Fluid Mech.* **116**, 157.

LIEPMANN, H. W., BROWN, G. L. & NOSENCHUCK, D. M. Control of laminar-instability waves using a new technique. *J. Fluid Mech.* **118**, 187.

LII, K. S., ROSENBLATT, M. & VAN ATTA, C. 1976 Bispectral measurements in turbulence. *J. Fluid Mech.* **77**, 45–62.

MANGANO, R. 1987 Transition of a boundary layer: controlled fundamental–subharmonic interactions. M.S. thesis, Illinois Institute of Technology.

MIKSAD, R., JONES, F. & POWERS, E. 1983 Measurements of nonlinear interactions during natural transition of a symmetric wake. *Phys. Fluids* **26**, 1402.

MIKSAD, R. W., JONES, F. L., POWERS, E. J., KIM, Y. C. & KHADRA, L. 1982 Experiments on the role of amplitude and phase modulations during transition to turbulence. *J. Fluid Mech.* **123**, 1–29.

SARIC, W. S. & THOMAS, A. S. W. 1984 Experiments on the subharmonic route to turbulence in boundary layers. In *Proc. IUTAM Symp. on Turbulence and Chaotic Phenomena in Fluids, Kyoto, Japan, Sept. 5–12.*

SINGER, B., FERZIGER, J. & REED, H. 1986 Investigation of the effects of initial disturbances on plane channel transition. *AIAA Paper* 86-0433.

SOLIS, R., MIKSAD, R. & POWERS, E. 1986 Experiments on the influence of mean flow unsteadiness on the laminar–turbulent transition of a wake. In *Proc. Tenth. Symp. on Fluids in Liquids, Rolla, Missouri.*

WILLIAMS, D., FASEL, H. & HAMA, F. R. 1984 Experimental determination of the three-dimensional vorticity field in the boundary-layer transition process. *J. Fluid Mech.* **149**, 179.